Parsing the Heterogeneity of Brain Metabolic Disturbances in Autistic Spectrum Disorder

Supplemental Information

Supplemental Methods and Materials

Participants

Recruitment, diagnosis, and inclusion/exclusion criteria for participants are detailed elsewhere (1). Briefly, 78 individuals with ASD, aged 5-60 (Table 1) recruited from clinics and the community participated. The institutional review board of the New York State Psychiatric Institute approved the study and written informed consent was obtained. Participants were diagnosed *per* DSM-IV for autistic disorder, Asperger disorder, or pervasive developmental disorder not otherwise specified. Assessments included the Autism Diagnostic Interview–Revised (ADI-R) (2) in children and, in 66 ASD participants, the Autism Diagnostic Observation Schedule (ADOS) (3) in children and adults. The ADOS returned a Total Score and subscores for Restricted and Repetitive Behaviors and Social Affect symptoms. In 62 ASD and 67 TD participants, core ASD symptoms were additionally evaluated with the Social Responsiveness Scale (SRS) (4). The SRS returned a Total (Raw) Score and subscores for Social Awareness, Social Cognition, Social Communication, Social Motivation and Restricted Behaviors. Participants with identifiable genetic or metabolic abnormalities, history of neurologic injury, seizures in the last 6 months, contraindications to MRI, or inability to comply with procedures were excluded. In the ASD sample, 26 participants were taking one or more psychotropic medications at time of study (Table 1), and 52 were taking no medication. (Analyses of metabolite effects based on the various medication classes was not contemplated, as this would lead to cells with very small numbers of participants. There were no significant differences between the medicated and unmedicated ASD subsamples in ADOS, SRS, or FSIQ scores.)

Ninety-six TD controls matched to ASD by age and sex participated, recruited by telemarketing. A detailed clinical interview was performed including the Kiddie Schedule for Affective Disorders and Schizophrenia

for children or the Structured Clinical Interview for DSM-IV Axis I Disorders for adults. Individuals with current or previous psychiatric or neurological disorder were excluded. Controls were also screened using the Social Communication Questionnaire (5) and the SRS. All controls scored below threshold for ASD on these instruments. No control was taking prescription or over-the-counter medication. The time-intensive ADOS was not conducted in the TD sample. The full-scale intelligence quotient (FSIQ) was assessed in both groups (68 ASD, 93 TD) using the Wechsler Abbreviated Scale of Intelligence.

The ASD and TD samples did not differ significantly in sex distribution, age, or socioeconomic status (Table 1). Both samples consisted of 40-45% children and adolescents and the remainder adults with a preponderance in their 20s, then evenly distributed by decade. Significant clustering in the age-distributions of the ASD and TD samples was ruled-out using Hartigan's method (6). Mean FSIQ was 5.9% lower in ASD (independent T-test, $t = -0.17$, $p = 0.046$). We opted not to balance the groups for IQ since low IQ is a frequent, and very high IQ an occasional, characteristic of ASD; our goal of examining effects of IQ in ASD explicitly was better served by selecting a sample with a broad IQ range (consistent with ability to cooperate with procedures). By design, scores on all SRS scales were much higher in the ASD sample (all $t > 1.20$, $p < 10^{-6}$), reflecting greater expression of ASD symptoms. Given the possibility of multicollinearity between FSIQ and other symptom scales in the ASD sample, we examined the Pearson correlation between FSIQ and the other scales. FSIQ was found not to correlate significantly (all $p > 0.05$) with any scale or subscale except for ADOS—Social Awareness ($r = -0.254$, $p = 0.038$). Therefore, the correlation analyses between ADOS—Social Awareness and metabolite levels were run without including FSIQ as a covariate.

MR Acquisition

Structural MRI and proton MRS were acquired as described (1). Briefly, all data were collected at 3T (GE Signa) with an 8-channel surface coil. A member of the study team was positioned at the opening of the magnet bore encouraging each participant to remain perfectly still, and monitoring for compliance. As the multiplanar chemical shift imaging (MPCSI) sequence was acquired last in a series of pulse-sequences, most participants were asleep for MPCSI. Motion-parameter estimates for DTI and rsfMRI sequences acquired just before MPCSI did not differ

significantly between ASD and TD participants. No major scanner hardware upgrades occurred during the study. Additionally, ASD and TD participants were scanned in intermixed order to promote equivalence of scanner conditions, and rigorous testing of field homogeneity and shimming was conducted on a weekly basis to ensure stable scanner performance. MRIs were read by a radiologist to exclude clinically significant findings. Whole-brain T1-weighted (T1w) MRI was obtained from each participant using a 3D spoiled gradient recall (SPGR) pulse-sequence with repetition time/echo-time (TR/TE) of 24/5 ms, flip angle 11°, and 0.98x0.98x1.0 mm^3 voxels. The T1w scan was used to prescribe MPCSI and for offline segmentation of the brain into gray and white matter. An in-plane high-resolution "localizer" MRI was acquired in register with MPCSI with TR/TE = 300/10 ms and voxels 0.98x0.98x10 mm^3. The localizer was used to coregister and to normalize MPCSI data into the common coordinate space of a template brain. MRS was acquired in 6 axial-oblique slabs (with 2-mm gap) parallel to the anterior commissure-posterior commissure (AC-PC): one slab below, one slab containing, and 4 slabs above the AC-PC (Figure 1). We used a water-suppressed MPCSI MRS sequence (7) and second-order dynamic shimming with TR/TE=2800/144 ms and voxels 10x10x10 mm^3. Extracranial lipids were suppressed with 8 saturation bands around the brain. MPCSI runtime, including shimming, was 30 min. More conventional single-voxel ^1H MRS would have offered advantages such as more uniform shim, short-TE acquisition, and water-referencing of metabolite levels. MPCSI, in contrast, permits broad simultaneous multiregional sampling of the brain at high spatial-resolution within tolerable runtimes. The MPCSI sequence we used additionally employs dynamic shimming and whole-slab excitation. It affords wider coverage than more common 2D PRESS or 2D STEAM options with less signal-loss from spatial-interference as no spatial-refocusing pulses are used (7).

MR Post-Processing

MR data were processed blind to diagnosis group as described (1,8-9), summarized below.

Structural MRI. After correction for image-intensity variations (10), the brain was extracted from extracerebral tissues (11) in each SPGR volume. Then all participant brains were coregistered to an initial template using a similarity transform that maximized mutual information (12), followed by a high-dimensional, nonrigid fluid-flow algorithm (13) that warped each brain to the exact size and shape of the template. Brain tissue was then segmented into gray and white matter using a semi-automated method (14).

MPCSI. MPCSI data were processed separately for each of the 8 coils before combination into spectroscopic images (15). Our very rigorous quality assurance for MR spectra in each of the 8 channels for each voxel ensured that motion did not confound our dataset. In addition to rejection of individual spectra of poor quality, MPCSI data were rejected *in toto* for 20 participants due to excessive head motion. (These participants are not included in the study sample size of 78 ASD and 96 TD.) For the remaining participants, first, we phase-aligned the signals, smoothed them with a Hamming filter, spatially reconstructed the time-domain free induction decay (FID) in each slab using 2D Fourier transform, suppressed residual water using singular-value decomposition (16), performed 4-Hz line broadening, then brought the time-domain signal into the frequency domain with 1D Fourier transform. Finally, we combined the signals from the 8 coils into a weighted sum (17). We loaded the combined signal into the in-house 3DiCSI software package, identified MPCSI voxels inside the brain, and saved spectral data for those voxels. We fit the frequency-domain signal to identify peaks for NAA (2.01 ppm), Glx (2.3-2.4 ppm), Cr (3.01 ppm), Cho (3.24 ppm), and lipids. Spectra were modeled with Gaussian-Lorentzian curves using least-squares. Areas under the fitted curves estimated metabolite concentrations in each voxel. We quality controlled the data by visually inspecting each spectrum, rejecting data from voxels with strong lipid contamination, insufficient water suppression, lack of separation between the Cr and Cho principal resonances, or full width at half maximum > 12 Hz. Visual inspection was preferred to the use of automated rejection of spectra exceeding a fixed Cramer-Rao Lower Bounds (CRLB) value. CRLB, however, were calculated for sample ASD spectra

passing inspection and were in the ranges: 7.5-8.2% for NAA, 17.1-18.6% for Glx, 13.4-16.1% for Cr, and 9.8-11.7% for Cho, all under the widely adopted 20% cut-off. We then computed background noise for the MR spectrum as the standard deviation of the real part of the complex spectrum free from metabolite signal, and calculated the signal-to-noise ratio (SNR) for each metabolite. Sample metabolite maps at native resolution are shown in Figure S1E. Average SNR for NAA was > 280, an excellent value attributable to the 8-channel surface coil and the use of noise from the (relatively flat) major-resonance-free portion of the spectrum. The Glx signal, often poorly visible above baseline at TE144, was better resolved than expected in this dataset. This was again attributed to the custom surface coil and the MPCSI sequence (less signal loss due to refocusing, more signal averaging with the long runtime). Additionally, phase and frequency of spectra were carefully adjusted for each individual coil before summing across coils. The more common summing without such adjustment can efface the Glx peak hindering fitting. We then generated a spectroscopic image for each metabolite as the ratio of peak area to background noise for each voxel, adjusted for variations in receiver and transmitter gain and calibrated to a series of phantom scans (8). These adjusted-calibrated ratios are proportional to actual metabolite levels. and were treated as such in cross-participant and cross-group comparisons.

We subsequently processed the spectroscopic images to correct for partial-voluming in each MPCSI voxel and for dispersion of the MRS signal into neighboring voxels (the point-spread function, PSF). Partial-voluming refers to the fact that an MRS voxel may contain more than one tissue type – e.g., gray matter and white matter – and that the signal in that voxel is a proportionate combination of signals from each component tissue. To estimate the proportions of gray and white matter in each MPCSI voxel, first, the SPGR was coregistered onto the localizer. Using the transform created by this coregistration, the gray-matter and white-matter component volumes of the SPGR were then coregistered into the localizer space, which is the same as the MPCSI space. The MPCSI PSF was independently estimated by simulating (8) the acquisition of MRS data on a 24x24 grid in k-space and then spatially filtering the simulated data with a Hamming window. The resulting 24x24 complex array was interpolated to 256x256, i.e., to SPGR resolution. The gray-and white-matter components were then convolved with this high-resolution PSF array to blur them to the low MPCSI resolution. We thence computed the fractions of gray and white matter (c_i^G, c_i^W) in each MPCSI voxel. These low-resolution

tissue-fractions were combined with S_{ij}, the adjusted-calibrated ratio determined as described above for metabolite j in voxel i of the MPCSI dataset. The equation $S_{ij} = \left|c_i^G * M_{ij}^G + c_i^W * M_{ij}^W\right| + n$ (n being noise) was then solved by linear regression (8) across neighboring voxels to extract the gray-matter, M_{ij}^G, and white-matter, M_{ij}^W, metabolite levels in each MPCSI voxel. We then trilinearly resampled M_{ij}^G and M_{ij}^W to the resolution of the study template (see below), which is the SPGR resolution, during spatial normalization. Thereby, an endpoint metabolite level was generated in each voxel in template space by summing the M_{ij}^G and M_{ij}^W values of neighboring MPCSI voxels, each weighted by its distance from the template voxel and the gray-matter or white-matter probability, respectively, of the template voxel. These endpoint metabolite levels were the values used in regression analyses. Note that partial-volume correction of local metabolite levels takes place at the low PSF-blurred MPCSI resolution. Similar to the smoothing kernel in BOLD fMRI, the PSF acts thereby as a spatial filter that removes any variations at higher-than-genuine spatial-frequency. It is only after this filtering that the data are interpolated and combined into cross-participant statistical parametric maps (SPMs). Higher-resolution features that subsequently appear on the SPMs thus result from cross-participant effects, rather than from within-participant interpolation.

Spatial Normalization of MPCSI. We co-registered the MPCSI volume for each participant into the coordinate space of a T1w template brain volume. We selected the template in two-steps (18). Briefly, as preliminary template, we selected the brain of an individual who was demographically representative of the cohort, then we nonlinearly warped each participant's brain to that initial template. Next, from the participant brains warped to the initial template, we selected as the final template the brain that was morphologically closest in the least-squares sense to the average brain across all participants. We then repeated coregistration and nonlinear warping of all brains to the final template brain. The choice of a study-specific brain template represented a middle-ground between using a single external standard adult template and using multiple age-specific child (19) and adult (20) templates. The former is simple, but coarse; the latter is precise, but complex. Ultimately it was decided that, while the extra precision of multiple age-specific templates would be appreciated in a study of brain

morphometry, it is not essential for present purposes of computing MPCSI voxel tissue-content, where the nominal spatial resolution far exceeds the spatial extent of regional variations in morphology reported in prior anatomical ASD imaging studies. Similarly, age-related differences in registration error to the template are likely too fine to impact MPCSI results.

We coregistered the metabolite images into the coordinate space of the template as follows: First, we coregistered each participant's localizer to its corresponding high-resolution T1w volume using a similarity transform (3 translations, 3 rotations) that maximized mutual information (12) across the localizer and its corresponding T1w. Second, we spatially transformed the localizer using the similarity transform that coregistered the T1w volume of the participant into the coordinate space of the template. Third, we warped the coregistered localizer by applying high-dimensional, nonlinear deformation that had warped the participant's T1w volume to the T1w template. We applied these procedures to each metabolite image.

This MPCSI-MRI co-analysis is analogous to standard fMRI post-processing, wherein one acquires data at low BOLD resolution, smoothes with a kernel to still lower resolution, then interpolates to high MRI resolution to display cross-participant statistical effects on SPMs. Certainly, the degree of interpolation is higher for MPCSI, but the principle is precisely the same. Furthermore, FDR in our method is applied not at MPCSI but at the higher MRI resolution which counters possible inflation of false positives. For MPCSI, we have validated this method by comparison with results at native MPCSI resolution (21) and at the region-of-interest level (9). Metabolite SPM values also correlate meaningfully with higher native resolution BOLD and DTI endpoints (8). Other groups have also successfully used CSI interpolated onto structural MRI (22-23). In interpreting metabolite SPMs, it is important to understand that they are statistical in character and portray cross-participant distributions rather than individual-participant spectroscopic images, i.e, SPMs give us the average locations of findings. Such findings are still useful for understanding ASD, even if their high resolution is not yet realizable on the single-participant level. Present methods are particularly useful because they afford rigorous within-participant correction of metabolite levels for partial-volume effects and a more uniform assignment of MPCSI voxels to homologous brain regions across participants.

Statistical Analyses

We covaried for age and sex in all statistical analyses of metabolite levels and conducted hypothesis testing at each voxel in the brain. To control for false positives (Type 1 error) we applied a False Discovery Rate (FDR) procedure (24) at FDR = 0.05; *p*-values that survived FDR correction were color-coded using warm-tones for positive, cool-tones for negative associations and displayed on the T1w template. Axial-oblique (AC-PC parallel) sections of the template were carefully compared with sections of the MNI152 brain and the best correspondence of *z*-levels was established for every 1-mm slice. The anatomic location of each effect on each metabolite map was then identified by expert opinion assisted by the Harvard-Oxford Atlas overlaid in the background of the MNI152 brain in FSLView. For cingulate subregions, the more accurate Vogt nomenclature (25) was substituted for the Harvard-Oxford labels.

Effects of Diagnosis and Symptoms. We assessed whether ASD relative to TD participants had abnormal levels of brain metabolites, using the multiple linear regression model $y_i = \beta_0 + \beta_1 \cdot \mathrm{Age}_i + \beta_2 \cdot \mathrm{Sex}_i + \beta_3 \cdot \mathrm{FSIQ}_i + \beta_4 \cdot \mathrm{Dx}_i + \epsilon_{ij}$, where $\mathrm{Dx}_i = 0$ for TD, 1 for ASD; $\mathrm{Sex}_i = 0$ for female, 1 for male; and y_i is the level of metabolite i. Effects of diagnosis ("Dx") were evaluated. An FSIQ term was included due to the slightly, but significantly, lower IQ in the ASD sample. We also assessed whether metabolite levels were associated with symptom severity in the ASD sample with the model $y_i = \beta_0 + \beta_1 \cdot \mathrm{Age}_i + \beta_2 \cdot \mathrm{Sex}_i + \beta_3 \cdot \mathrm{Sx}_i + \varepsilon_i$, where Sx_i is severity (ADOS or SRS Total or subscale score) in participant i.

Effects of Age. In the combined (ASD+TD) sample, we assessed effects of age on metabolite levels using the model $y_{ij} = \beta_0 + \beta_1 \cdot \mathrm{Age}_i + \beta_2 \cdot \mathrm{Sex}_i + \beta_3 \cdot \mathrm{Dx}_i + \beta_4 \cdot \mathrm{Dx}_i * \mathrm{Age}_i + \varepsilon_{ij}$. Effects of the diagnosis-by-age interaction ("Dx*Age") were evaluated to identify where in the brain age correlates differed significantly in ASD *vs.* TD participants, or equivalently where differences across groups varied with age. Subsequently, we assessed effects of age on metabolite levels in the ASD sample alone using the model $y_{ij} = \beta_0 + \beta_1 \cdot \mathrm{Age}_i + \beta_2 \cdot \mathrm{Sex}_i + \varepsilon_{ij}$, and effects of age were evaluated in voxels where we detected a significant diagnosis-by-age interaction.

Effects of Sex. In the combined sample, we assessed effects of sex on metabolites using the model $y_{ij} = \beta_0 + \beta_1 \cdot \mathrm{Age}_i + \beta_2 \cdot \mathrm{Sex}_i + \beta_3 \cdot \mathrm{Dx}_i + \beta_4 \cdot \mathrm{Dx}_i * \mathrm{Sex}_i + \varepsilon_{ij}$. Effects of the diagnosis-by-sex interaction term were evaluated to identify where in the brain group differences varied by sex. Subsequently, we assessed effects of sex on metabolites in the ASD sample alone using the model $y_{ij} = \beta_0 + \beta_1 \cdot \mathrm{Age}_i + \beta_2 \cdot \mathrm{Sex}_i + \varepsilon_{ij}$, and effects of the sex term were evaluated in voxels where we detected a significant diagnosis-by-sex interaction. Finally, given the higher incidence of ASD in males than in females, we compared metabolites between the two participant groups using male participants only and the model $y_{ij} = \beta_0 + \beta_1 \cdot \mathrm{Age}_i + \beta_2 \cdot \mathrm{Dx}_i + \varepsilon_{ij}$.

Effects of FSIQ. In the combined sample, we assessed effects of participant FSIQ on metabolites using the model $y_{ij} = \beta_0 + \beta_1 \cdot \mathrm{Age}_i + \beta_2 \cdot \mathrm{Sex}_i + \beta_3 \cdot \mathrm{Dx}_i + \beta_4 \cdot FSIQ_i + \beta_5 \cdot \mathrm{Dx}_i * FSIQ_i + \varepsilon_{ij}$. Effects of the diagnosis-by-FSIQ interaction were evaluated to identify where in the brain group differences varied with FSIQ, or equivalently where the FSIQ correlates of metabolites differed across groups. Subsequently, we assessed effects of FSIQ on metabolite levels in ASD alone and TD alone using $y_{ij} = \beta_0 + \beta_1 \cdot \mathrm{Age}_i + \beta_2 \cdot \mathrm{Sex}_i + \beta_3 \cdot \mathrm{FSIQ}_i + \varepsilon_{ij}$.

Selection of Metabolite Results For Comment. The metabolite maps below document numerous significant findings throughout the brain. To keep the figures uncluttered and the text concise, only major effects are labelled and mentioned in Results. Beyond being statistically significant after FDR-correction, all major effects satisfied two criteria. First, current use of any psychotropic medication was added as a covariate to all analyses that included ASD participants. All such analyses were repeated excluding all ASD participants on medication (see figures below). Findings were considered major and are reported in the main text only for those cases that were significant both covarying for medication *and* excluding medicated participants. Second, findings were considered major and are reported in the main text only if they were significant for a majority volume (as judged by eye) of the brain region in question. Thus, the focus was on robust and salient findings. That being said, any colored portion of any metabolite map is statistically significant and the interested reader is at liberty to identify further, minor findings.

The reader is advised that the *z*-levels depicted vary in the figures below. In each figure, a selection of slices is displayed rather than all slices scanned. The latter option would have produced very small, cramped maps with many slices showing only minor or no significant effects at all. The present configuration of *z*-levels has been selected such that all major effects as defined above are displayed. Moreover, partial matching of *z*-levels has been implemented such that the same effect can be examined on the same slices across maps for the full sample *vs.* the unmedicated subsample and that interactions can be compared to main effects on the same slices. Complete maps showing all slices are available from the authors upon request. Also note that, for most cases with significant bilateral effects, although reported for both hemispheres in the text, labels are drawn over only one hemisphere on the figures. Finally, note in figure legends that the numbers of participants varied slightly from analysis to analysis depending on how many participants had usable ADOS, SRS, or FSIQ scores.

Supplemental Results

Effects of ASD Diagnosis and Symptoms on MRS Metabolites

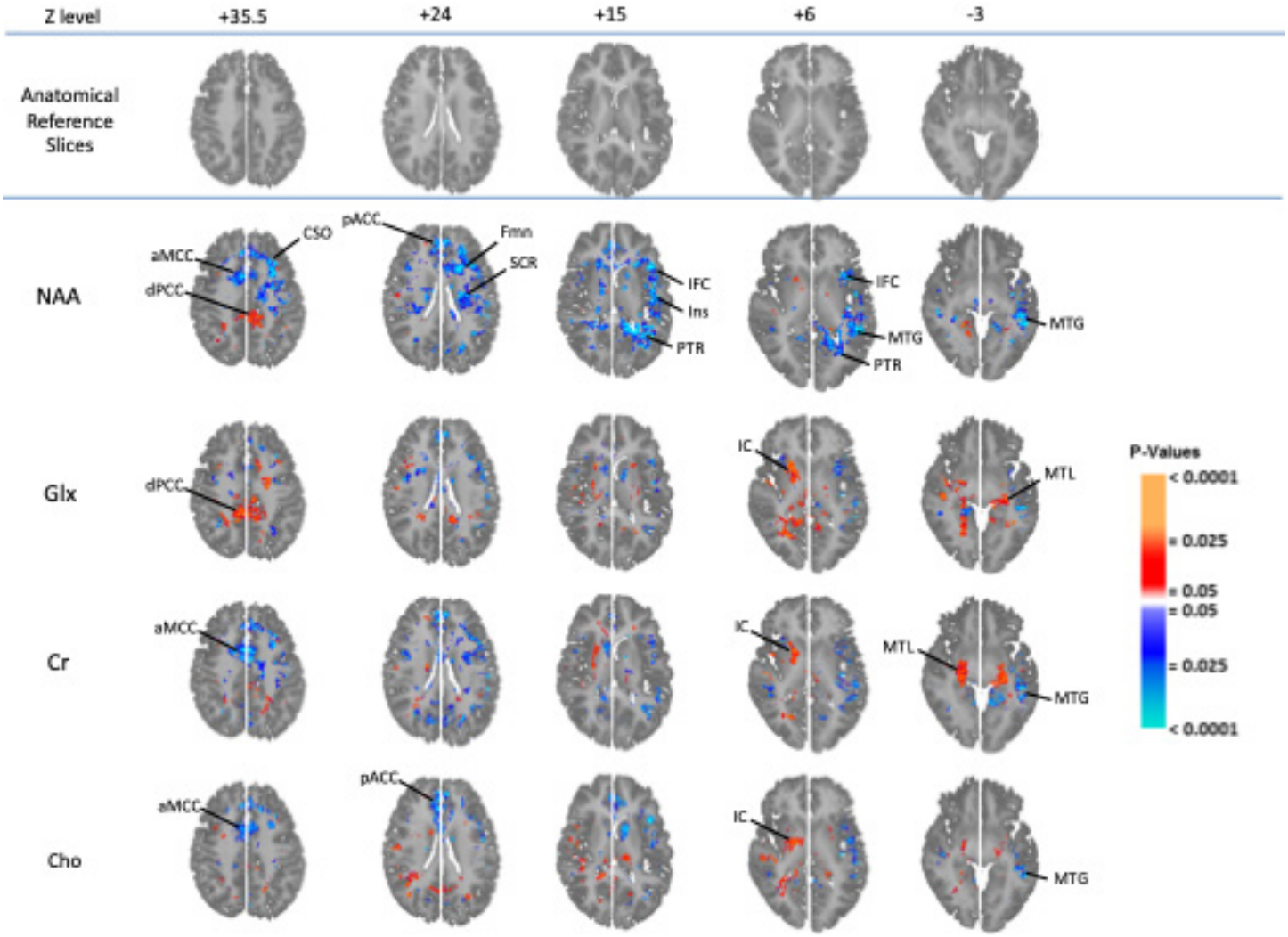

Figure S1. (A) Statistical parametric maps (SPMs) superimposed on axial-oblique MRI at selected Montréal Neurological institute z (superior-inferior) levels of the custom brain template for our participant sample showing regions where group-mean metabolite levels are higher (orange-red) and lower (cyan-blue) for the autistic spectrum disorder (ASD) than the typically developing (TD) control sample, covarying for age, sex, full-scale intelligence quotient (FSIQ), and use of any psychotropic medications. Results are corrected for multiple comparisons using the false discovery rate (FDR) method. Analysis performed on usable data from 68 ASD and 93 control participants. In this and subsequent figures, labels are drawn only for regions for which the effect was significant both including and excluding participants on medication. For most cases with significant bilateral effects, labels are drawn over one hemisphere only. NAA, *N*-acetyl-compounds; Glx, glutamate plus glutamine; Cr, creatine plus phosphocreatine; Cho, choline compounds. aMCC, anterior middle cingulate cortex; CSO, centrum semiovale; dPCC, dorsal posterior cingulate cortex; FMn, forceps minor; IC, internal capsule; IFC, inferior frontal cortex; Ins, insula; MTG, middle temporal gyrus (cortex plus white matter); MTL, mesial temporal lobe (amygdala, hippocampus, parahippocampal cortex, rostral lingual cortex); pACC, pregenual anterior cingulate cortex; PTR, posterior thalamic radiations; SCR, superior corona radiata.

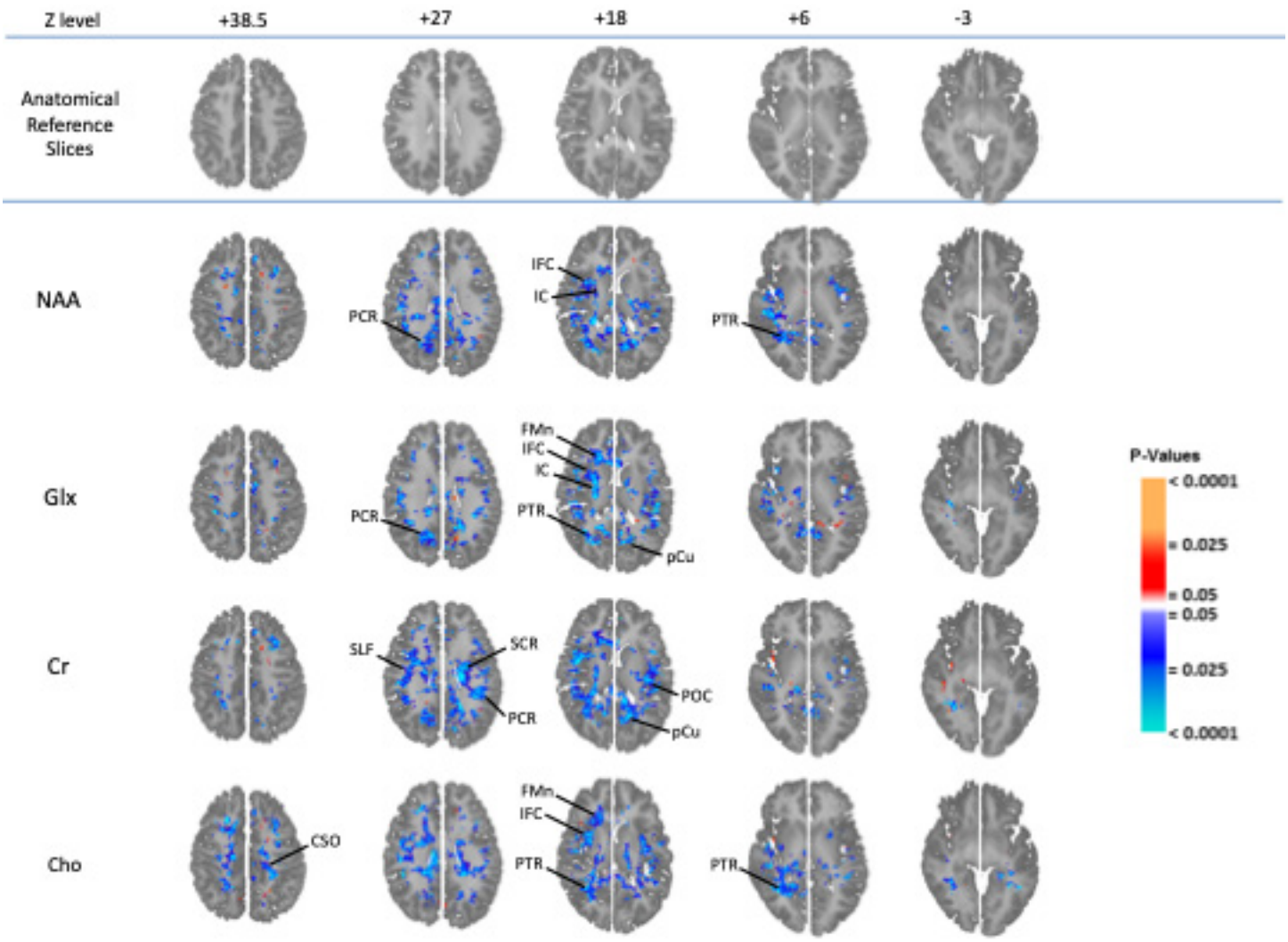

Figure S1. (B) Positive (orange-red) and inverse (cyan-blue) correlations of metabolite levels with core ASD symptoms as expressed by the Autism Diagnostic Observation Schedule (ADOS) Total Score covarying for age, sex, FSIQ, and use of any psychotropic medication (FDR-corrected); 68 ASD participants. pCu, precuneus; PCR, posterior corona radiata; POC, parietal opercular cortex; SLF, superior longitudinal fissure.

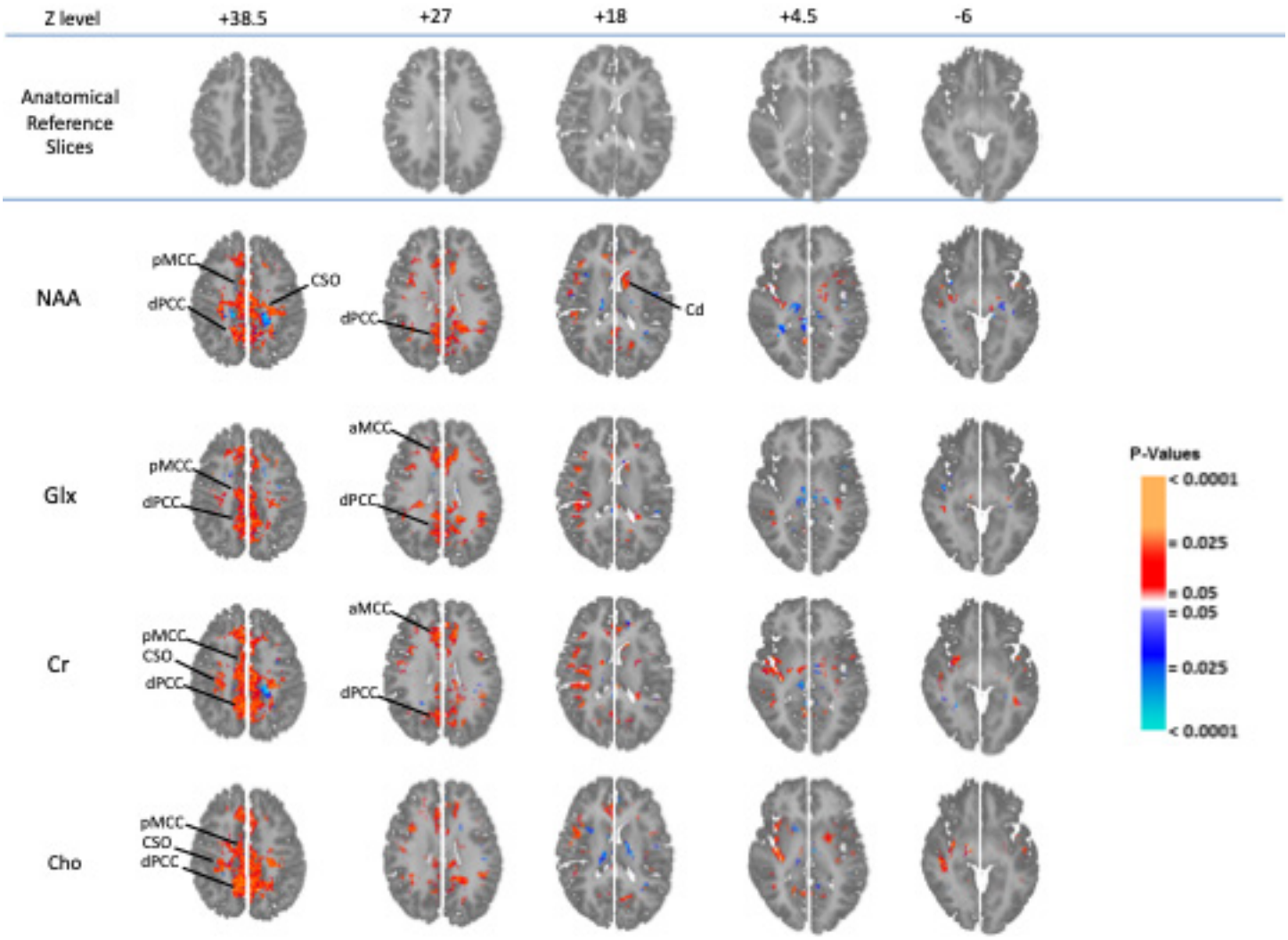

Figure S1 (C) Correlations of metabolites with core ASD symptoms as expressed by the Social Responsiveness Scale (SRS) Total Score covarying for age, sex, and use of any psychotropic medication (FDR corrected); 62 ASD participants. Cd, caudate nucleus; pMCC, posterior middle cingulate cortex.

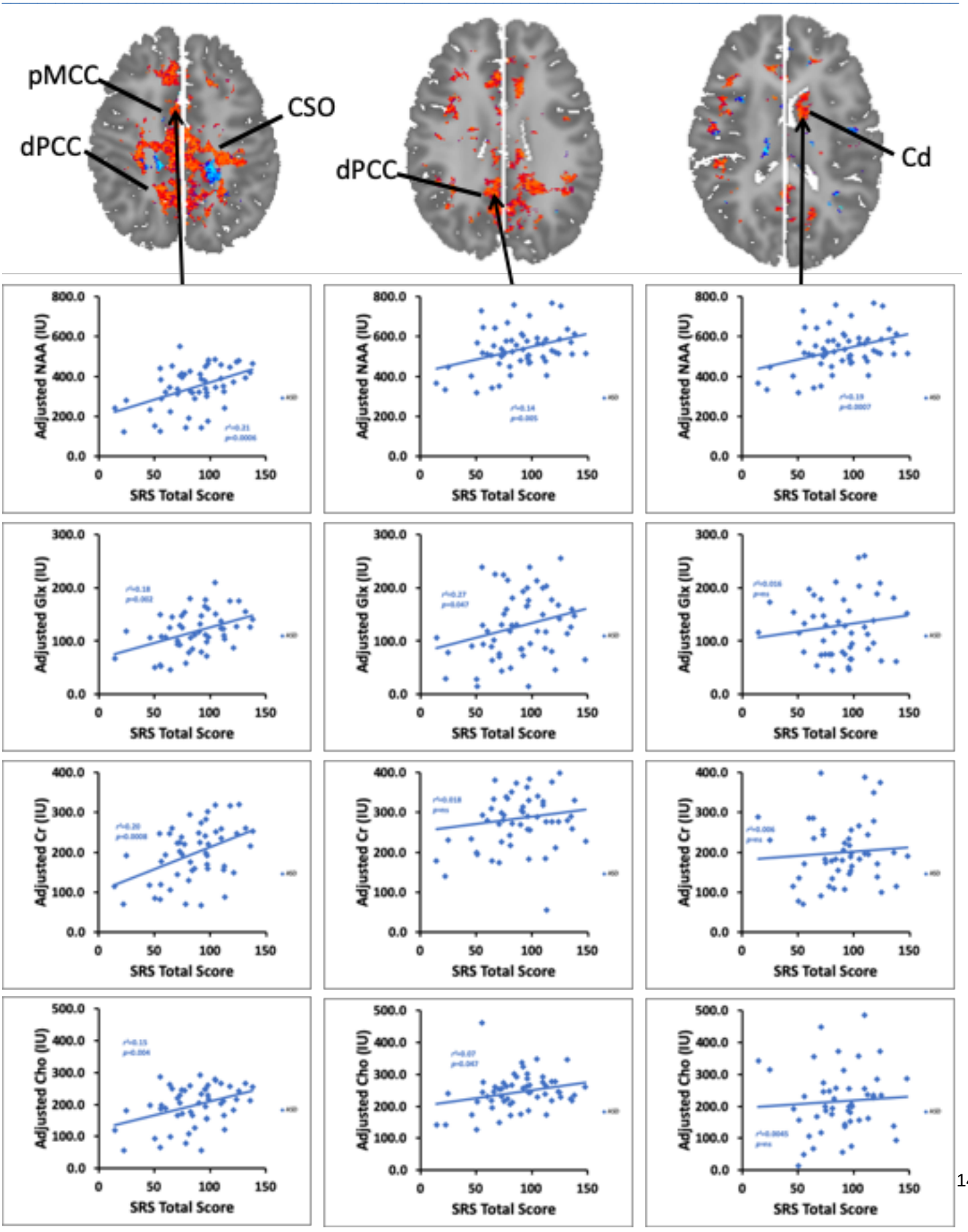
Z level
+38.5
+27
+18
pMCC
dPCC
CSO
dPCC
Cd
Adjusted NAA (IU)
Adjusted Glx (IU)
Adjusted Cr (IU)
Adjusted Cho (IU)
SRS Total Score

Figure S1. (D) Scatterplots at three representative voxels from panel (C) for NAA, Glx, Cr, and Cho to indicate relations between SRS Total Score and metabolite levels. Scatterplots were refit omitting outliers without appreciable change to the findings.

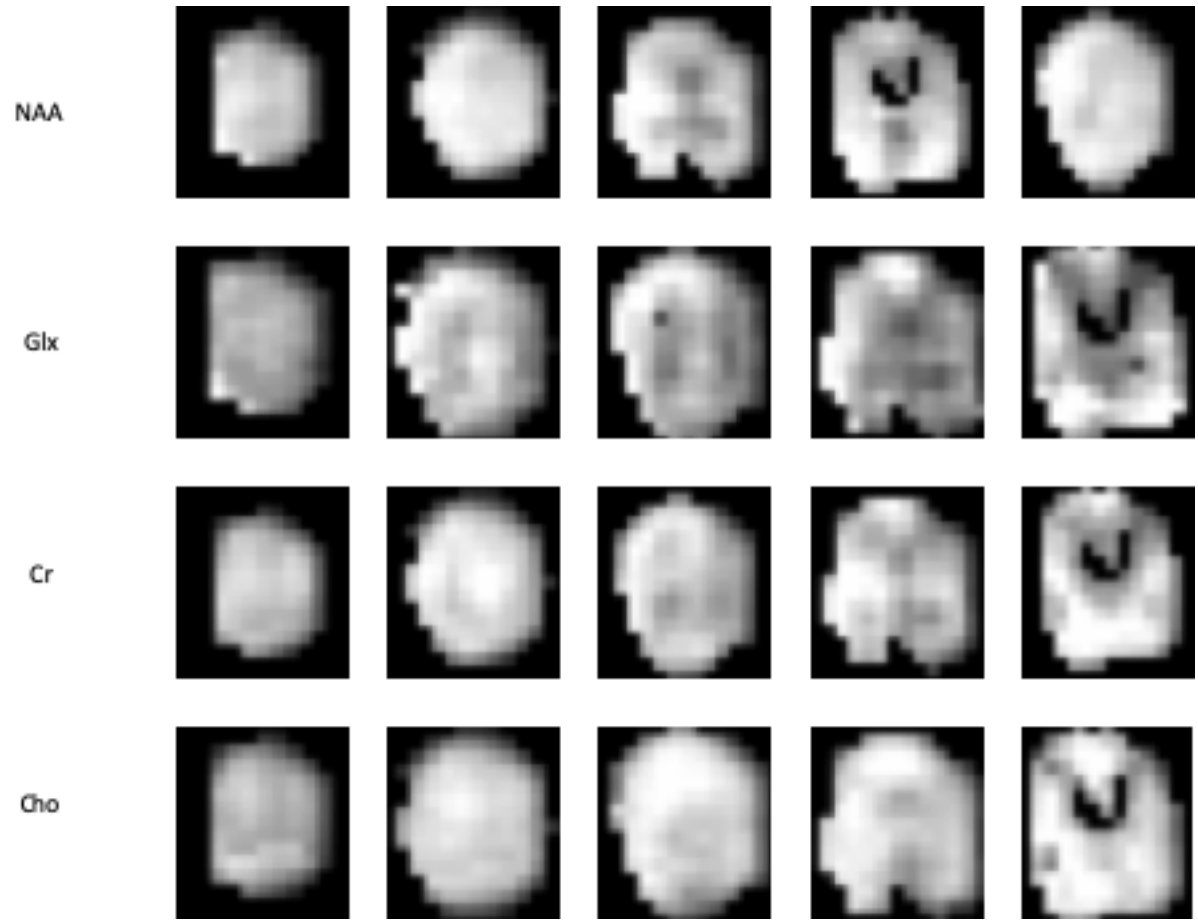

Figure S1. (E) Axial-oblique spectroscopic images at original MPCSI resolution for a representative ASD participant at various superior-inferior levels. Plotted are metabolite signal intensities normed to transmitter- and receiver-gain-corrected standard deviation of the noise in the metabolite-free region of the real part of the MR spectrum.

Table S1. Sample ASD and TD Regional Metabolite Levels (Effects from Fig. 1 ASD *v* TD)

	NAA		Glx		Cr		Cho	
	ASD	TD	ASD	TD	ASD	TD	ASD	TD
Left CSO	332 (189)	440 (187)	76 (51)	99 (54)	161 (95)	211 (85)	192 (124)	224 (99)
Right aMCC	248 (110)	355 (144)	92 (48)	117 (52)	167 (80)	235 (88)	171 (84)	238 (92)
Left dPCC	327 (120)	324 (143)	112 (51)	103 (48)	210 (79)	216 (90)	170 (70)	167 (75)
Right pACC	323 (159)	381 (158)	104 (62)	113 (56)	193 (87)	237 (115)	225 (121)	247 (106)
Left FMn	356 (104)	422 (114)	70 (31)	84 (35)	172 (52)	193 (63)	250 (83)	270 (88)
Left SCR	427 (126)	492 (126)	80 (31)	83 (30)	192 (57)	207 (58)	223 (72)	253 (74)
Left IFC	310 (142)	393 (132)	70 (40)	84 (44)	150 (76)	187 (71)	167 (99)	210 (100)
Left Ins	416 (157)	513 (182)	77 (40)	96 (44)	184 (81)	198 (65)	227 (95)	273 (84)
Left PTR	360 (188)	414 (142)	86 (53)	86 (32)	184 (99)	188 (67)	175 (100)	199 (91)

Values are metabolite intensities normed to transmitter- and receiver-gain-corrected standard deviation of the noise in the metabolite-free region of the MR spectrum. For abbreviations see Figure 1 ASD v TD.

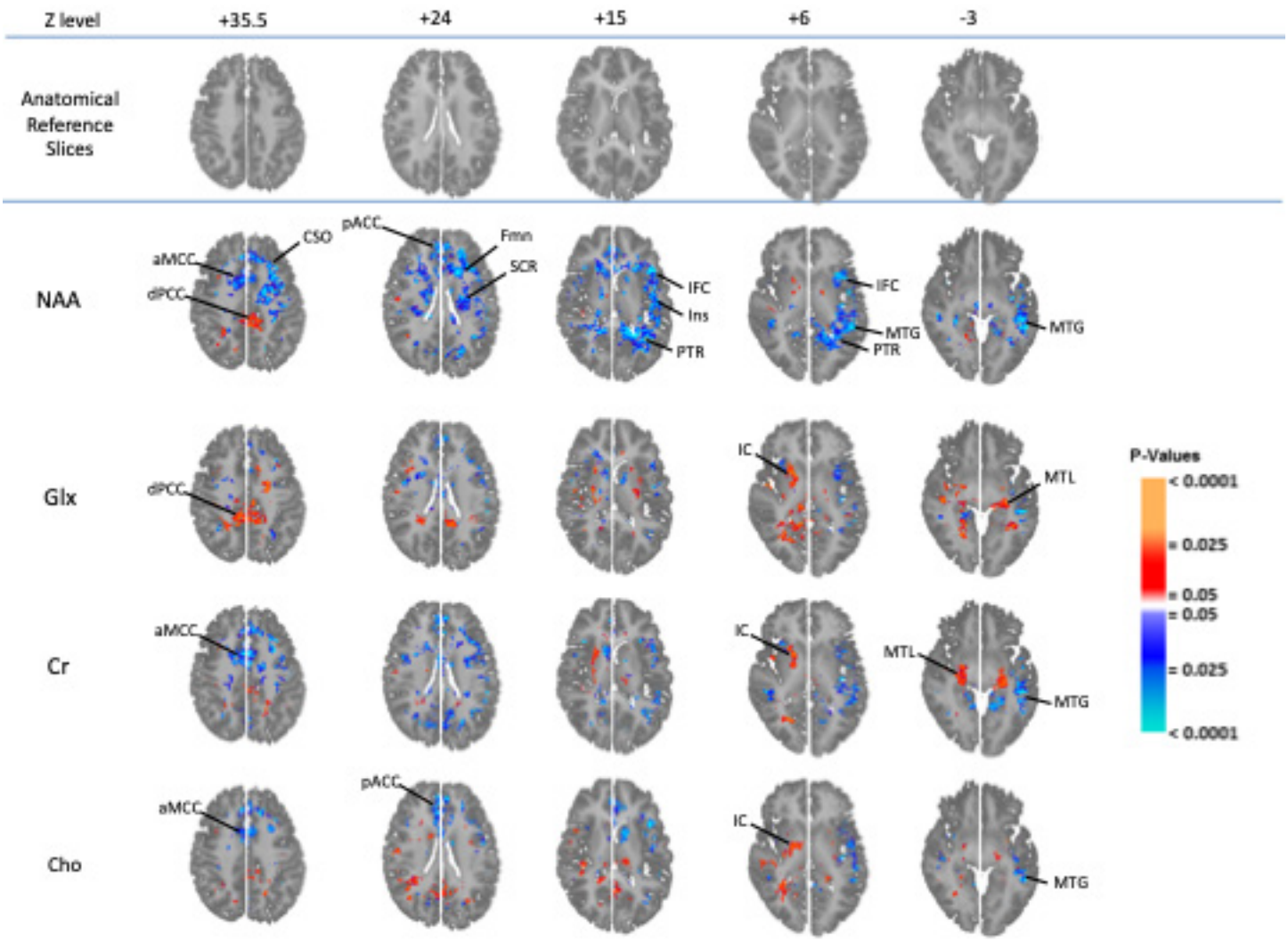

Figure S2 (A) Regions where group-mean metabolite levels are higher (orange-red) and lower (cyan-blue) for the ASD than the TD sample, covarying for age, sex and FSIQ (FDR corrected). Analysis performed on usable data from 44 *unmedicated* ASD and 93 TD participants. NAA, *N*-acetyl-compounds; Glx, glutamate plus glutamine; Cr, creatine plus phosphocreatine; Cho, choline compounds. aMCC, anterior middle cingulate cortex; CSO, centrum semiovale; dPCC, dorsal posterior cingulate cortex; FMn, forceps minor; IC, internal capsule; IFC, inferior frontal cortex; Ins, insula; MTG, middle temporal gyrus; MTL, mesial temporal lobe; pACC, pregenual anterior cingulate cortex; PTR, posterior thalamic radiations; SCR, superior corona radiata.

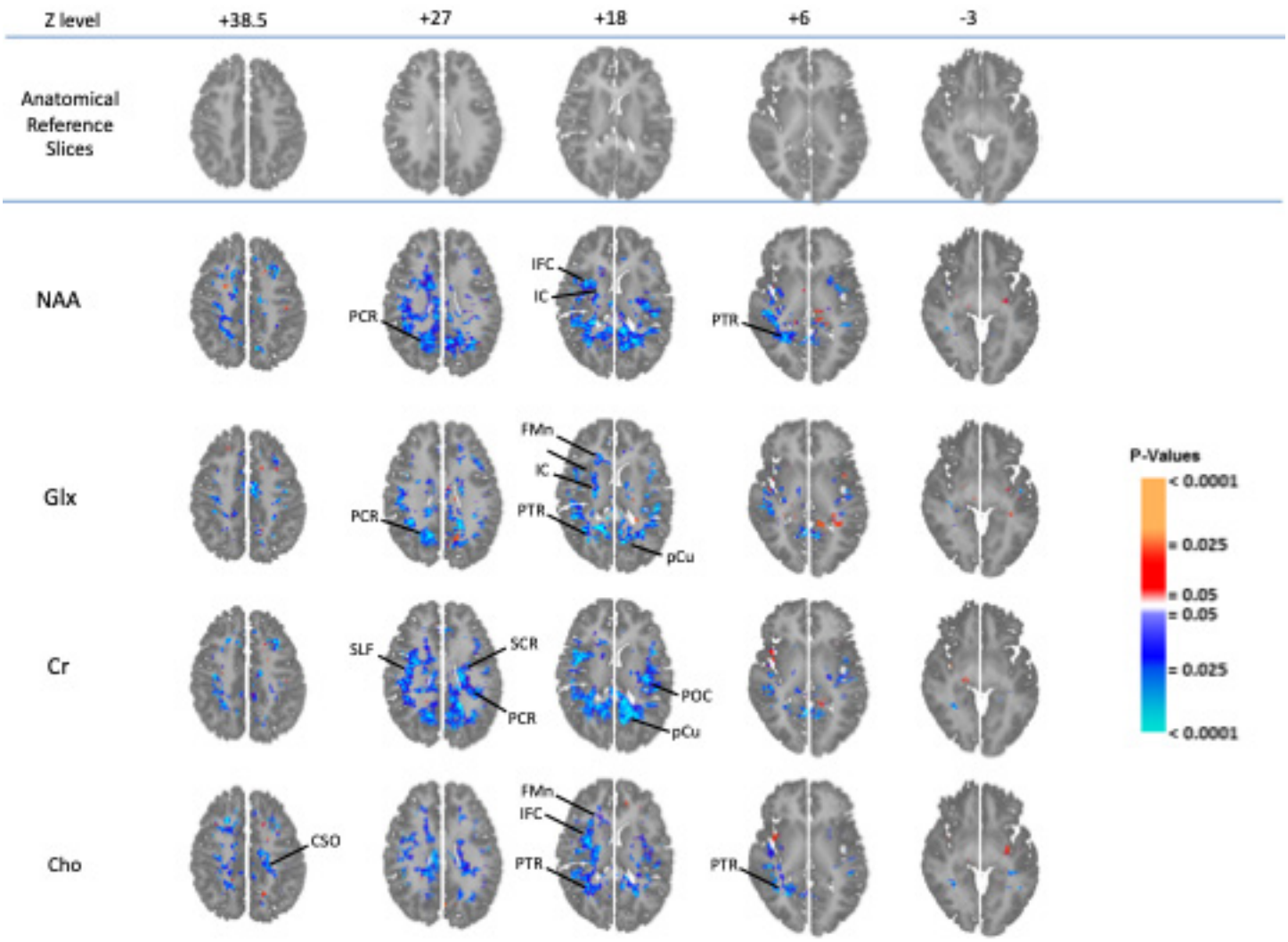

Figure S2 (B) Positive (orange-red) and inverse (cyan-blue) correlations of metabolites with core ASD symptoms expressed by the Autism Diagnostic Observation Schedule (ADOS) Total Score covarying for age, sex, and FSIQ (FDR corrected); 45 unmedicated ASD participants. pCu, precuneus; PCR, posterior corona radiata; POC, parietal opercular cortex; SLF, superior longitudinal fasciculus.

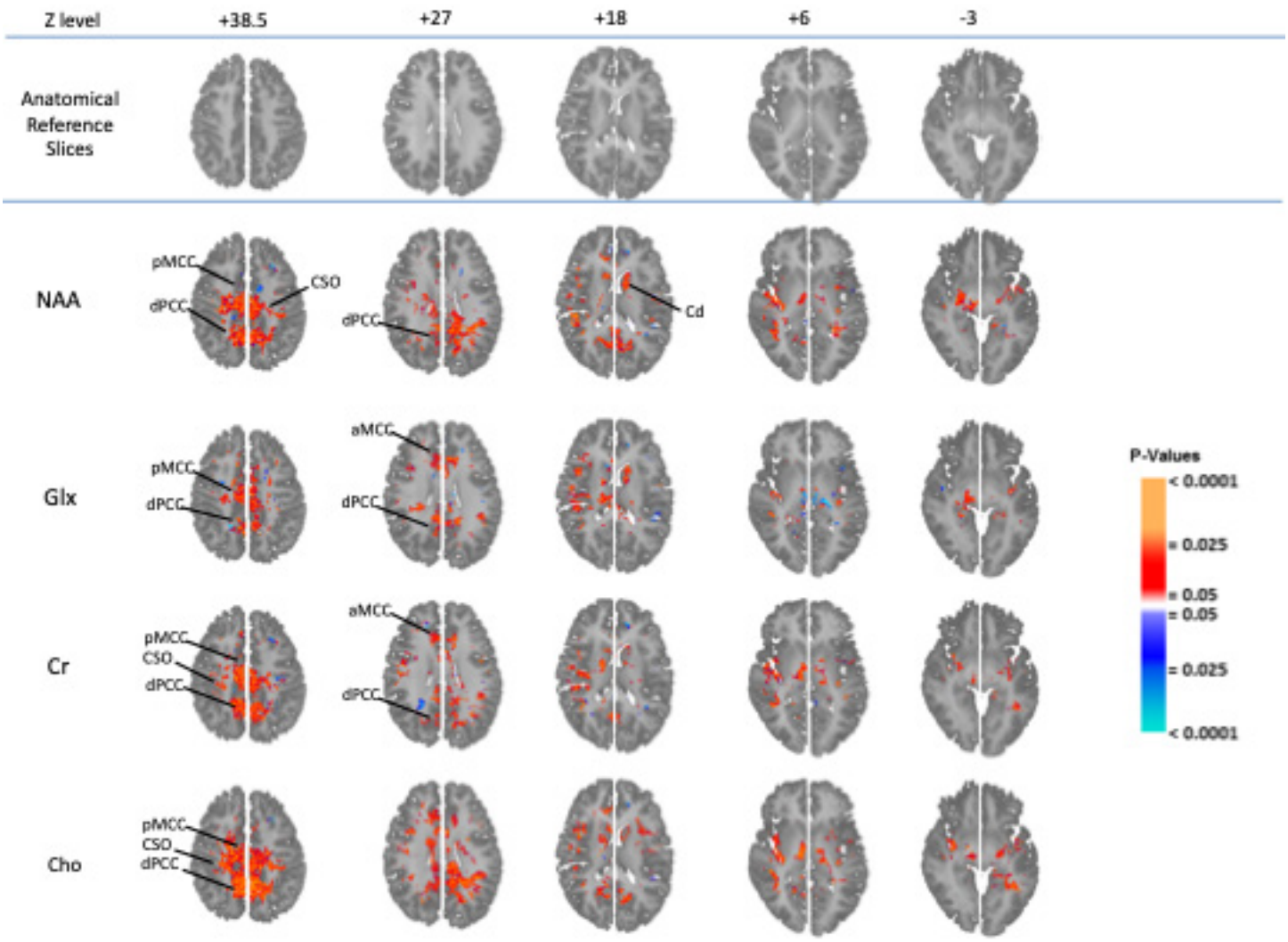

Figure S2 (C) Correlations of metabolites with core ASD symptoms expressed by the Social Responsiveness Scale (SRS) Total Score covarying for age, sex, and FSIQ (FDR corrected); 39 unmedicated ASD participants. Cd, caudate; pMCC, posterior middle cingulate cortex.

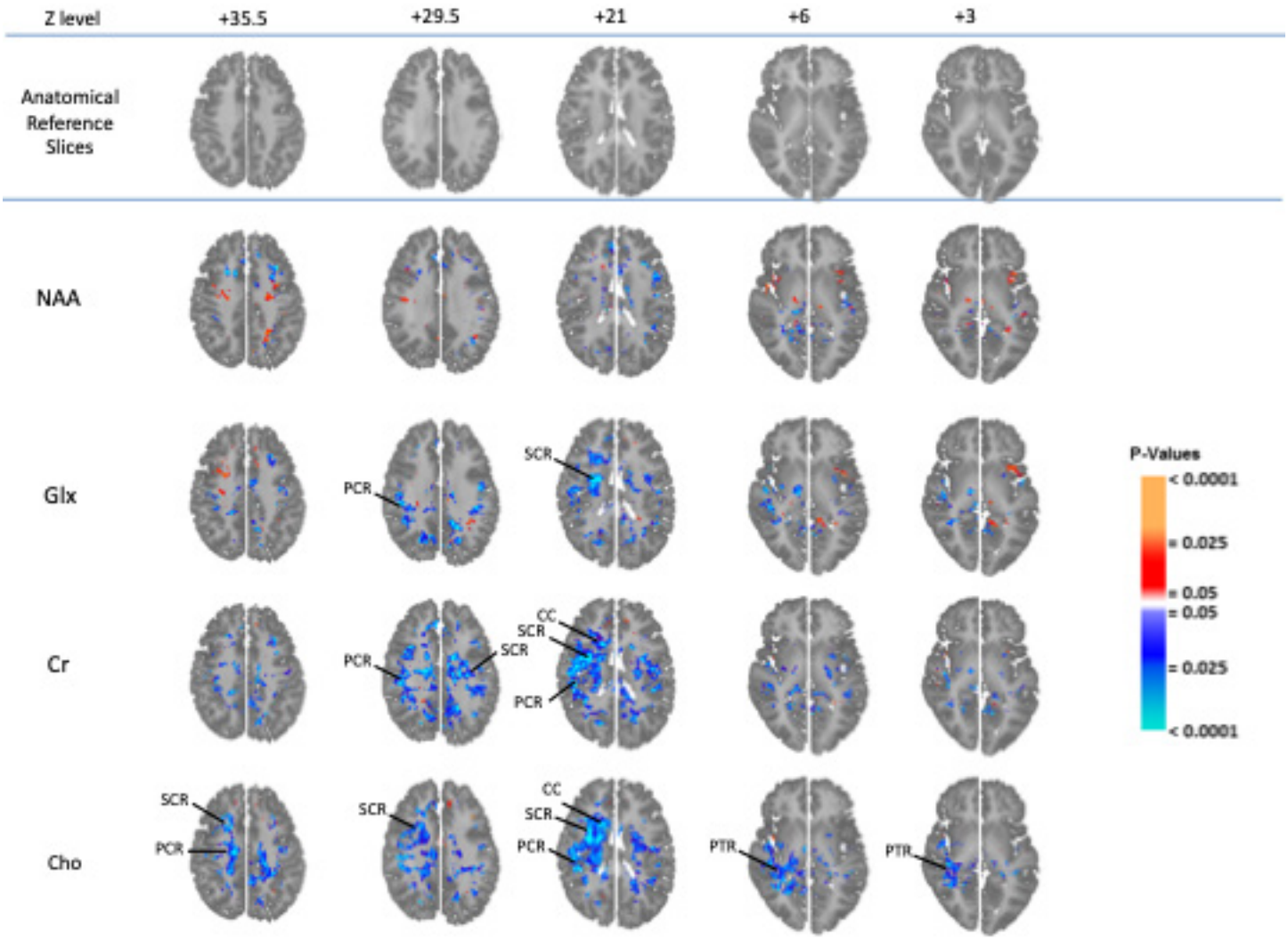

Figure S3 (A) Correlations of metabolites with the ADOS Social Affect symptoms subscale covarying for age, sex, FSIQ, and use of any psychotropic medication (FDR-corrected); 68 ASD participants. NAA, *N*-acetyl-compounds; Glx, glutamate plus glutamine; Cr, creatine plus phosphocreatine; Cho, choline compounds. CC, corpus callosum; PCR, posterior corona radiata; PTR, posterior thalamic radiations; SCR, superior corona radiata.

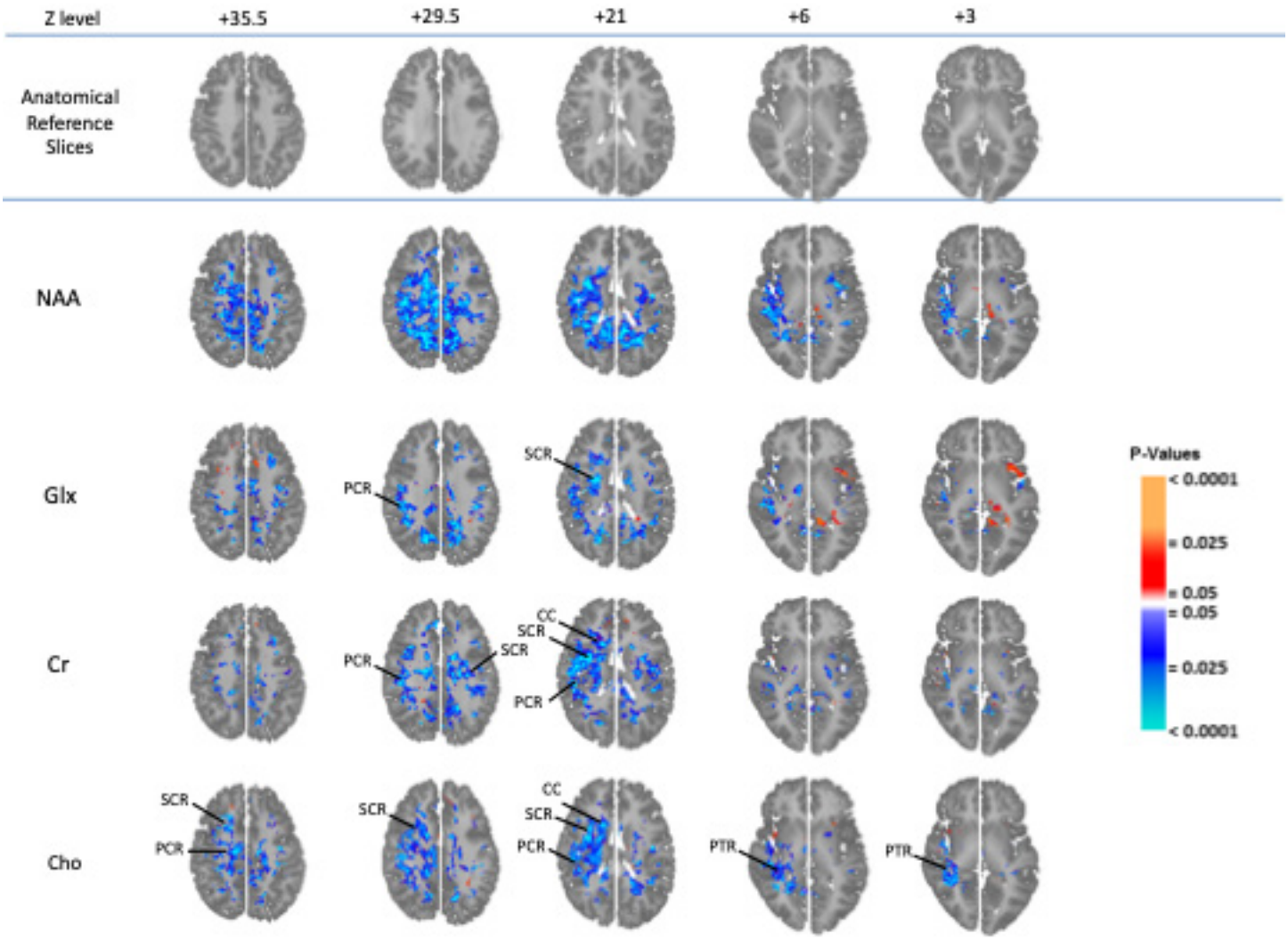

Figure S3 (B) Correlations of metabolites with the ADOS Social Affect symptoms subscale covarying for age, sex, and FSIQ (FDR-corrected); 45 unmedicated ASD participants.

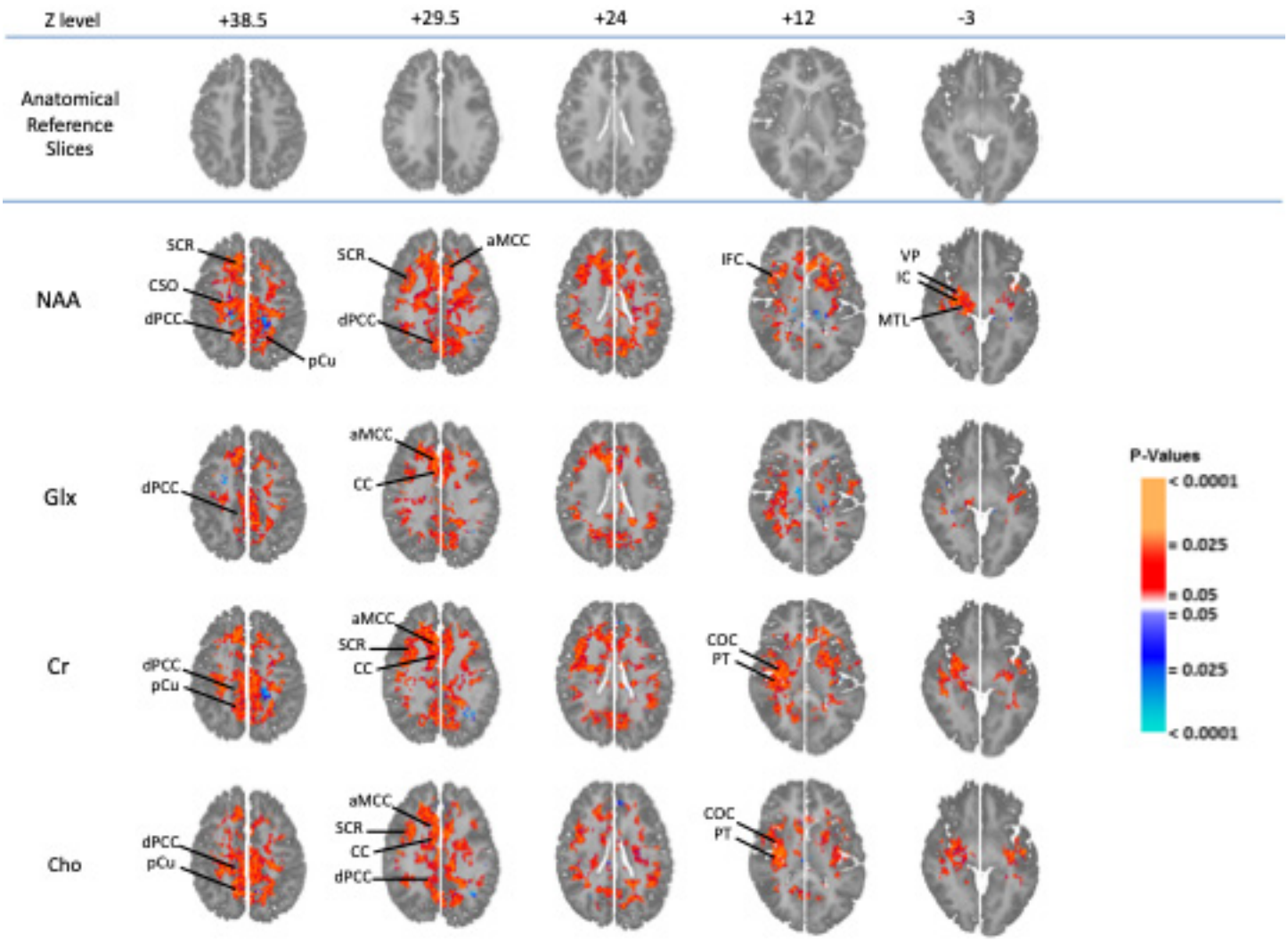

Figure S4 (A) Correlations of metabolites with the SRS Social Awareness symptoms subscale covarying for age, sex, FSIQ, and medication (FDR-corrected); 62 ASD participants. NAA, *N*-acetyl-compounds; Glx, glutamate plus glutamine; Cr, creatine plus phosphocreatine; Cho, choline compounds. aMCC, anterior middle cingulate cortex; CC, corpus callosum; COC, central opercular cortex; CSO, centrum semiovale; dPCC, dorsal posterior cingulate cortex; IC, internal capsule; IFC, inferior frontal cortex; MTL, mesial temporal lobe; pCu, precuneus; PT, planum temporale; SCR, superior corona radiata; VP, ventral pallidum.

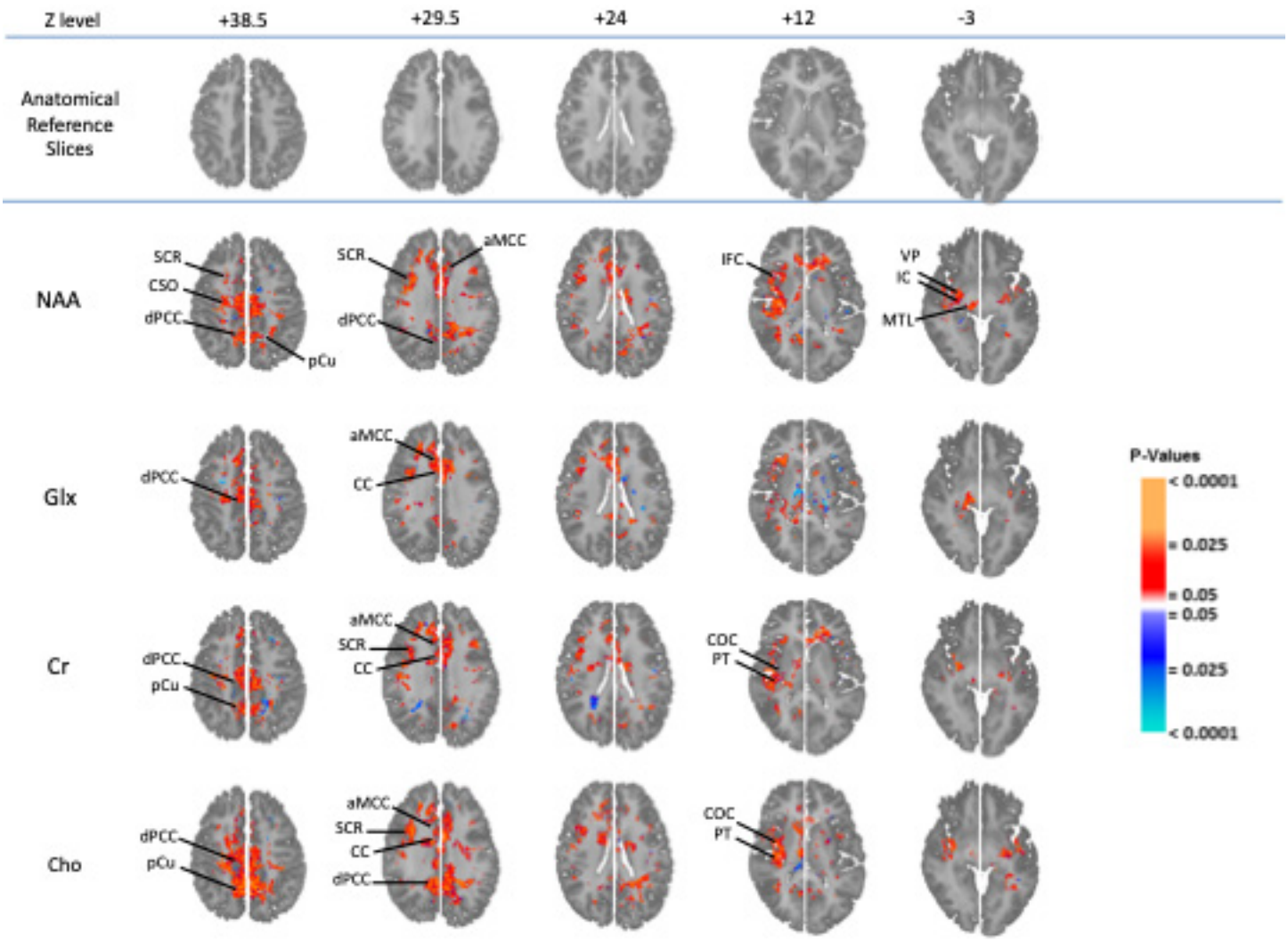

Figure S4 (B) Correlations of metabolites with the SRS Social Awareness symptoms subscale covarying for age, sex, and FSIQ (FDR-corrected); 39 unmedicated ASD participants.

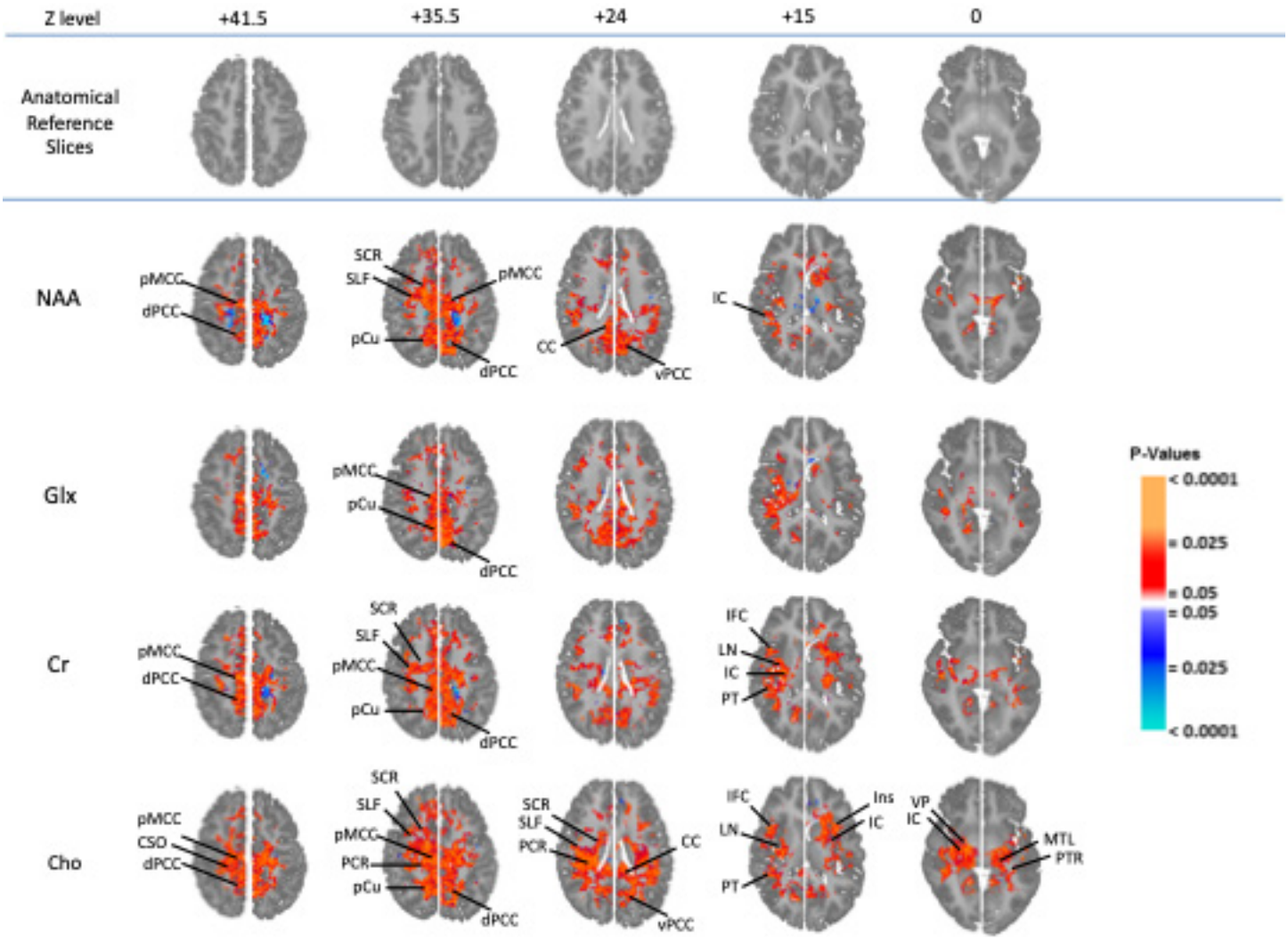

Figure S5 (A) Correlations of metabolites with the SRS Social Cognition symptoms subscale covarying for age, sex, FSIQ, and use of any psychotropic medication (FDR-corrected); 62 ASD participants. NAA, *N*-acetyl-compounds; Glx, glutamate plus glutamine; Cr, creatine plus phosphocreatine; Cho, choline compounds. CC, corpus callosum; CSO, centrum semiovale; dPCC, dorsal posterior cingulate cortex; IC, internal capsule; IFC, inferior frontal cortex; Ins, insula; LN, lenticular nucleus (putamen plus globus pallidus); MTL, mesial temporal lobe; PCR, posterior corona radiata; pCu, precuneus; pMCC, posterior middle cingulate cortex; PT, planum temporale; PTR, posterior thalamic radiations; SCR, superior corona radiata; SLF, superior longitudinal fasciculus; VP, ventral pallidum; vPCC, ventral posterior cingulate cortex.

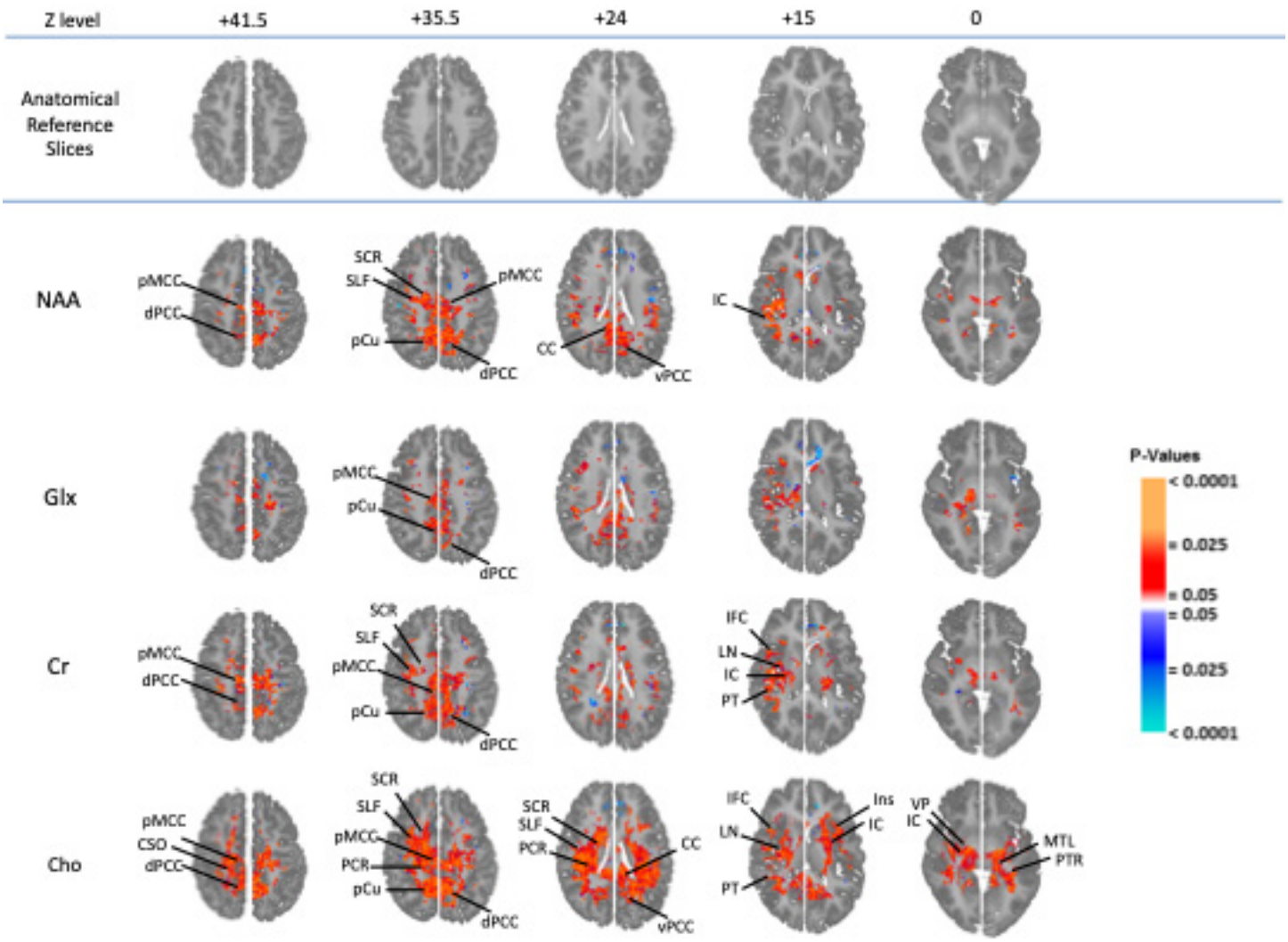

Figure S5 (B) Correlations of metabolites with the SRS Social Cognition symptoms subscale covarying for age, sex, and FSIQ (FDR-corrected); 39 unmedicated ASD participants.

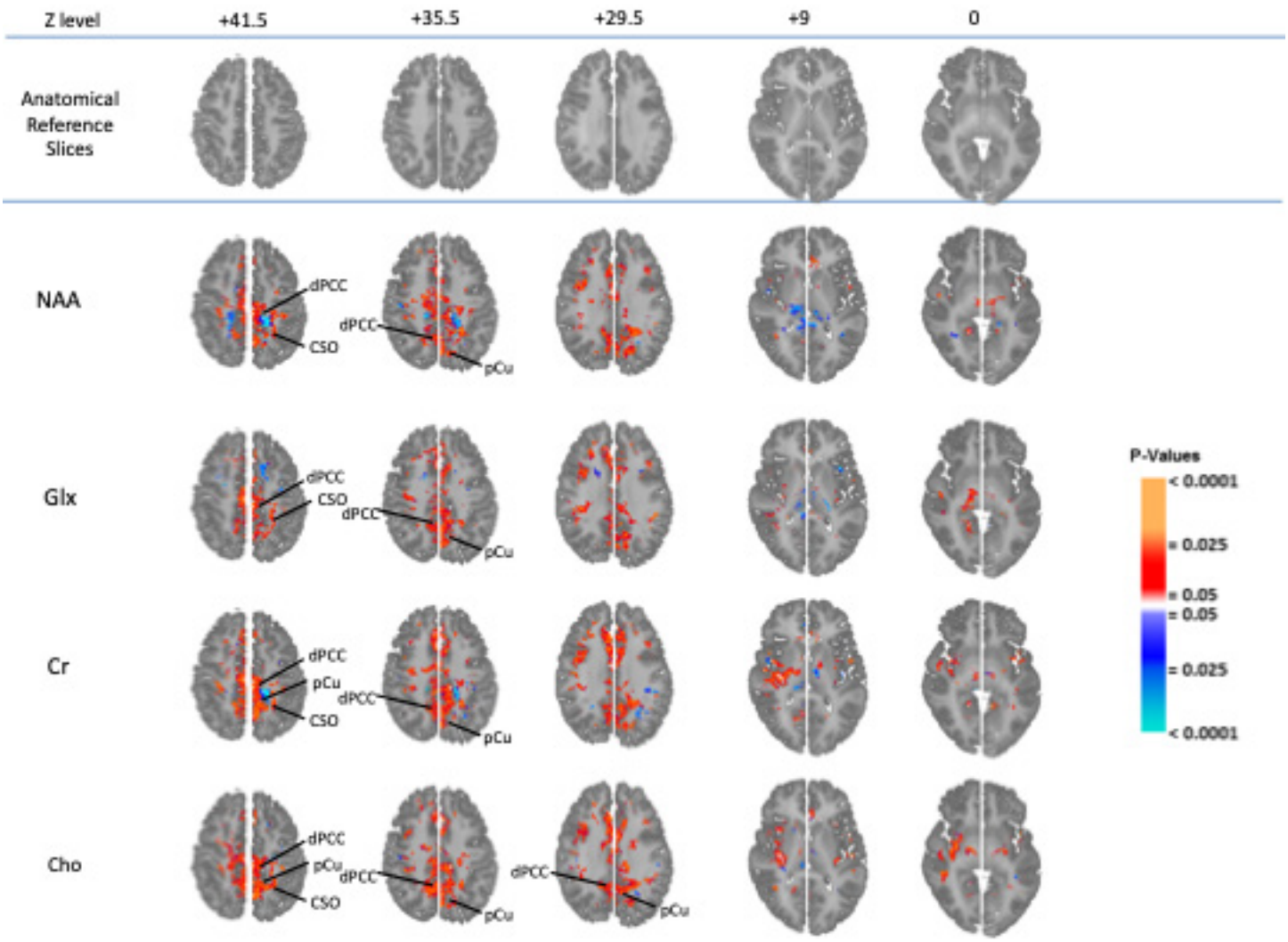

Figure S6 (A) Correlations of metabolites with the SRS Social Communication symptoms subscale covarying for age, sex, FSIQ and use of any psychotropic medication (FDR-corrected); 62 ASD participants. NAA, *N*-acetyl-compounds; Glx, glutamate plus glutamine; Cr, creatine plus phosphocreatine; Cho, choline compounds. CSO, centrum semiovale; dPCC, dorsal posterior cingulate cortex; pCu, precuneus.

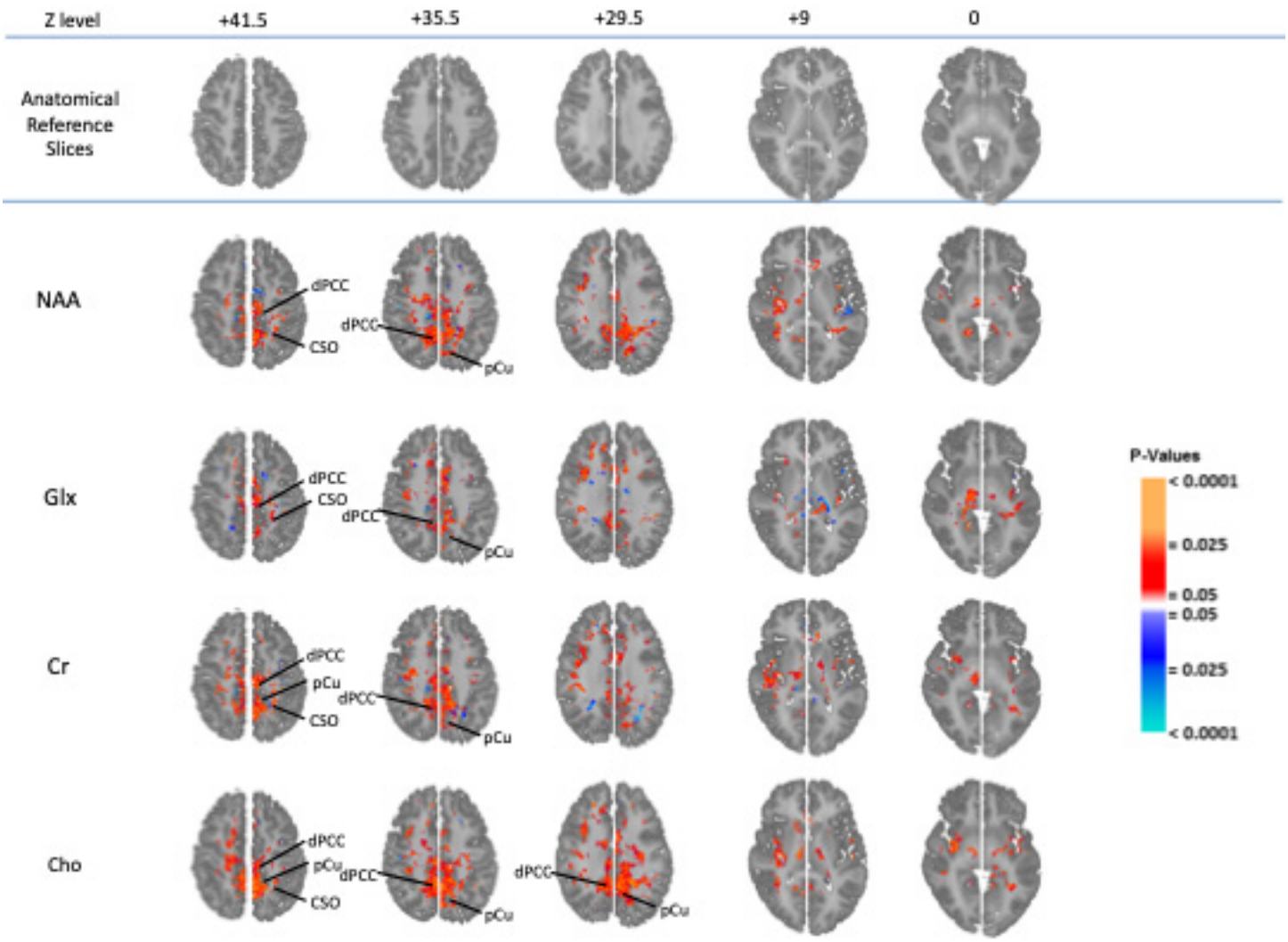

Figure S6 (B) Correlations of metabolites with the SRS Social Communication symptoms subscale covarying for age, sex, and FSIQ (FDR-corrected); 39 unmedicated ASD participants.

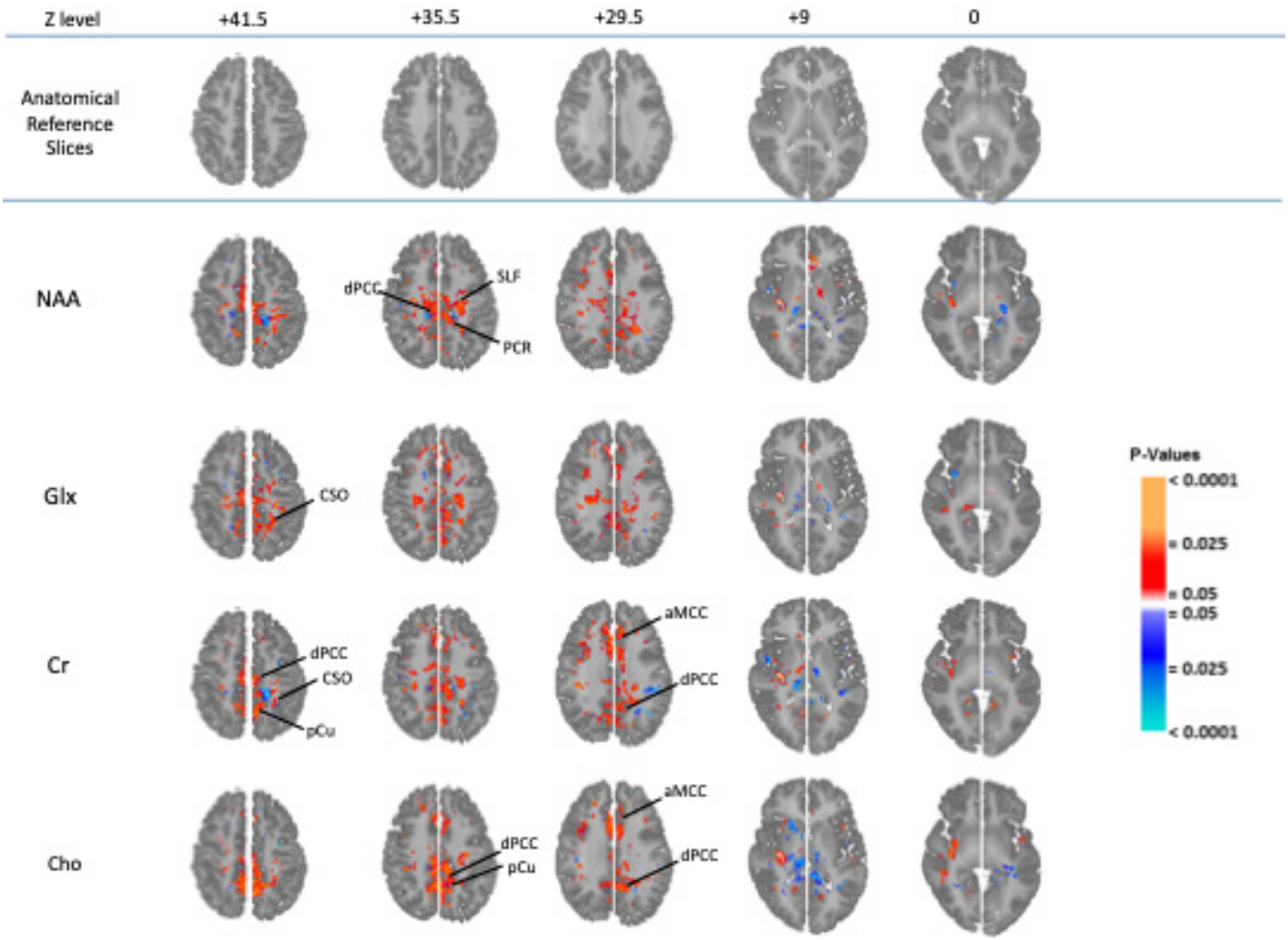

Figure S7 (A) Correlations of metabolites with the SRS Restricted Behavior symptoms subscale covarying for age, sex, FSIQ, and use of any psychotropic medication (FDR-corrected); 62 ASD participants. NAA, *N*-acetyl-compounds; Glx, glutamate plus glutamine; Cr, creatine plus phosphocreatine; Cho, choline compounds. aMCC, anterior middle cingulate cortex; CSO, centrum semiovale; dPCC, dorsal posterior cingulate cortex; PCR, posterior corona radiata; pCu, precuneus; SLF, superior longitudinal fasciculus; Ins, insula; MTG, middle temporal gyrus.

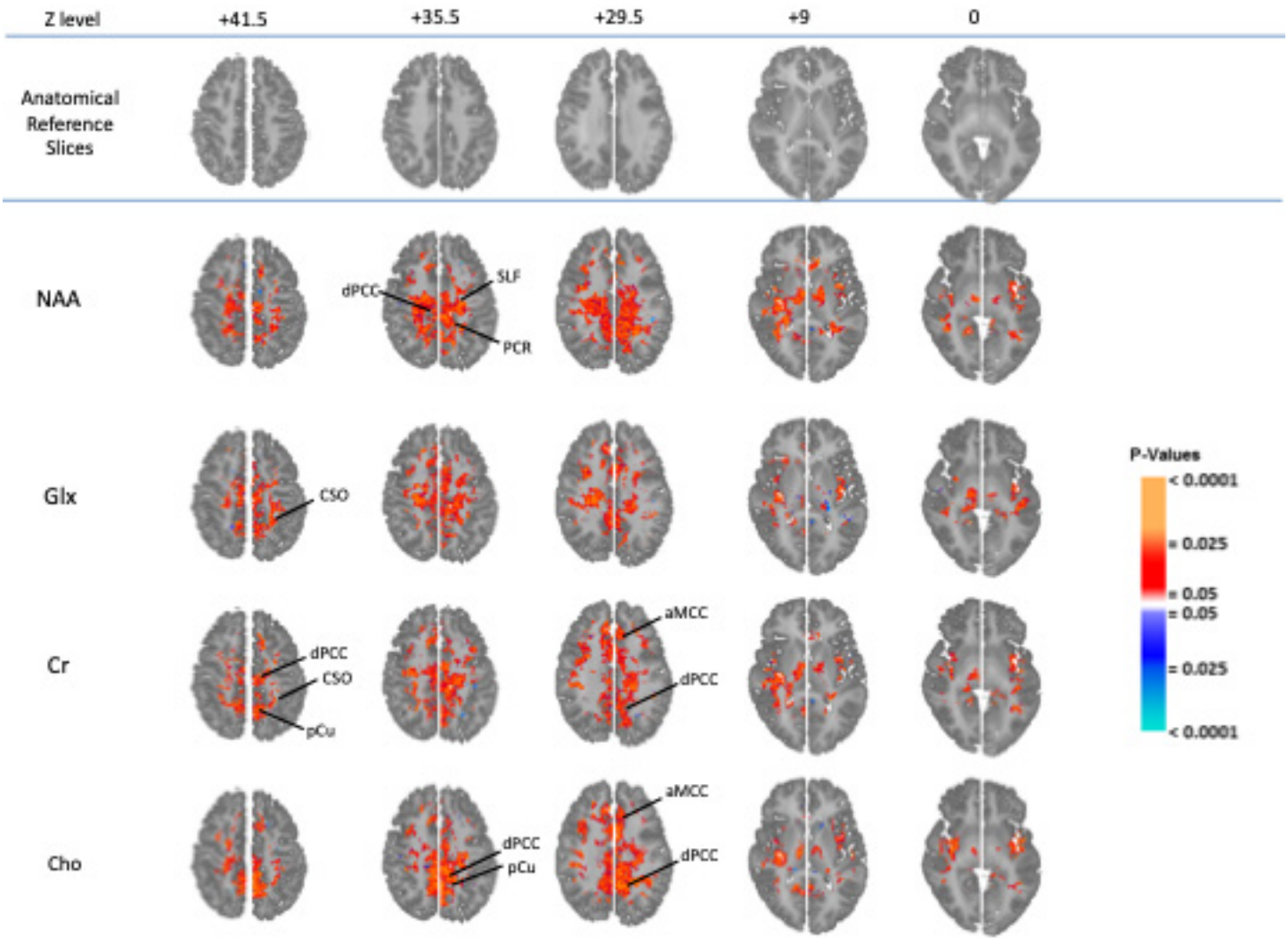

Figure S7 (B) Correlations of metabolites with the SRS Restricted Behavior symptoms subscale covarying for age, sex, and FSIQ (FDR-corrected); 39 unmedicated ASD participants.

Effects of Age, Sex, and FSIQ on MRS Metabolites

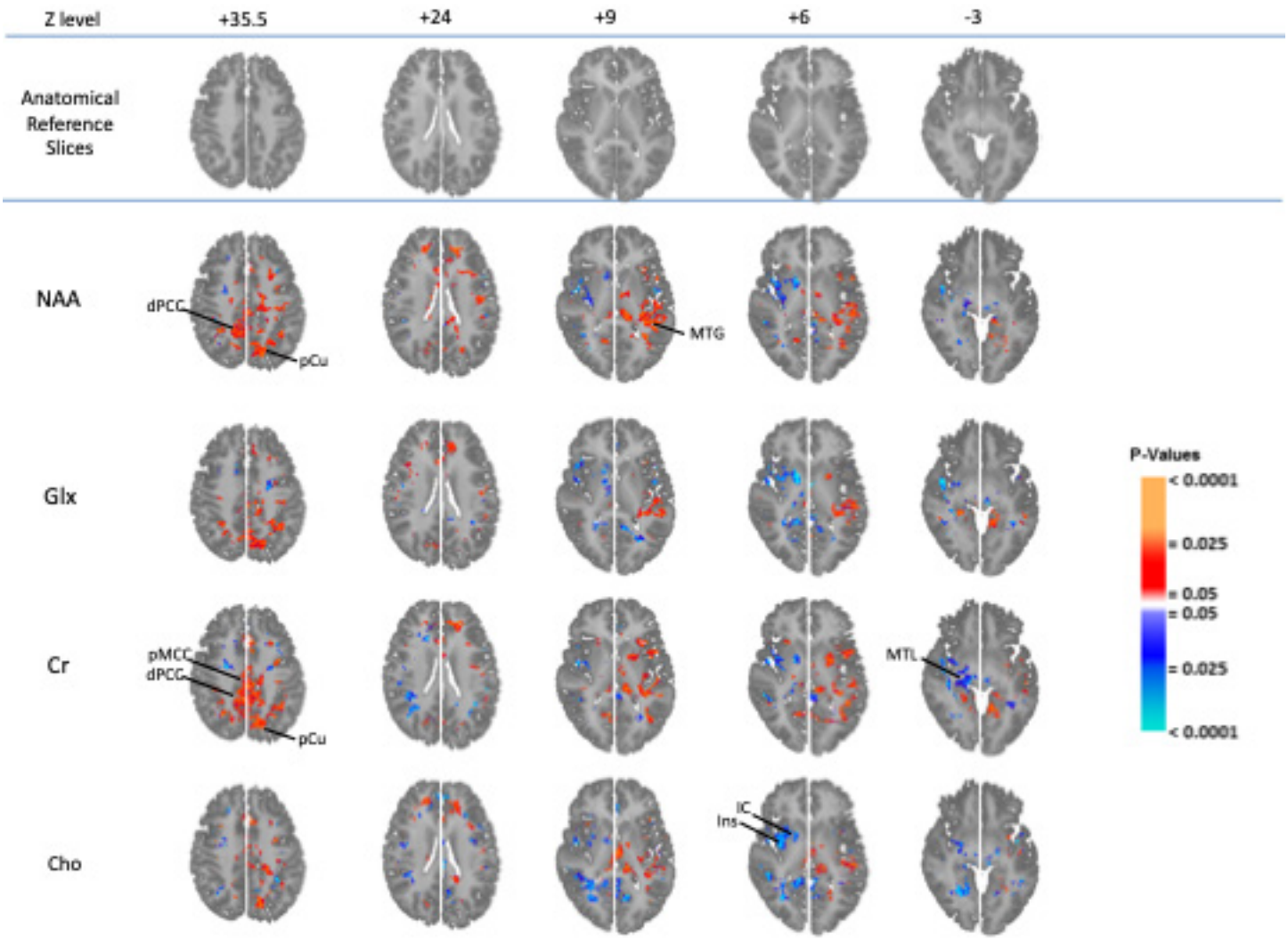

Figure S8 (A) Age-by-diagnosis interactions for metabolites covarying for sex, diagnosis, and use of any psychotropic medication (FDR corrected); 78 ASD, 96 TD participants. NAA, *N*-acetyl-compounds; Glx, glutamate plus glutamine; Cr, creatine plus phosphocreatine; Cho, choline compounds. dPCC, dorsal posterior cingulate cortex; IC, internal capsule; Ins, insula; MTG, middle temporal gyrus; MTL, mesial temporal lobe; pCu, precuneus; pMCC, posterior middle cingulate cortex.

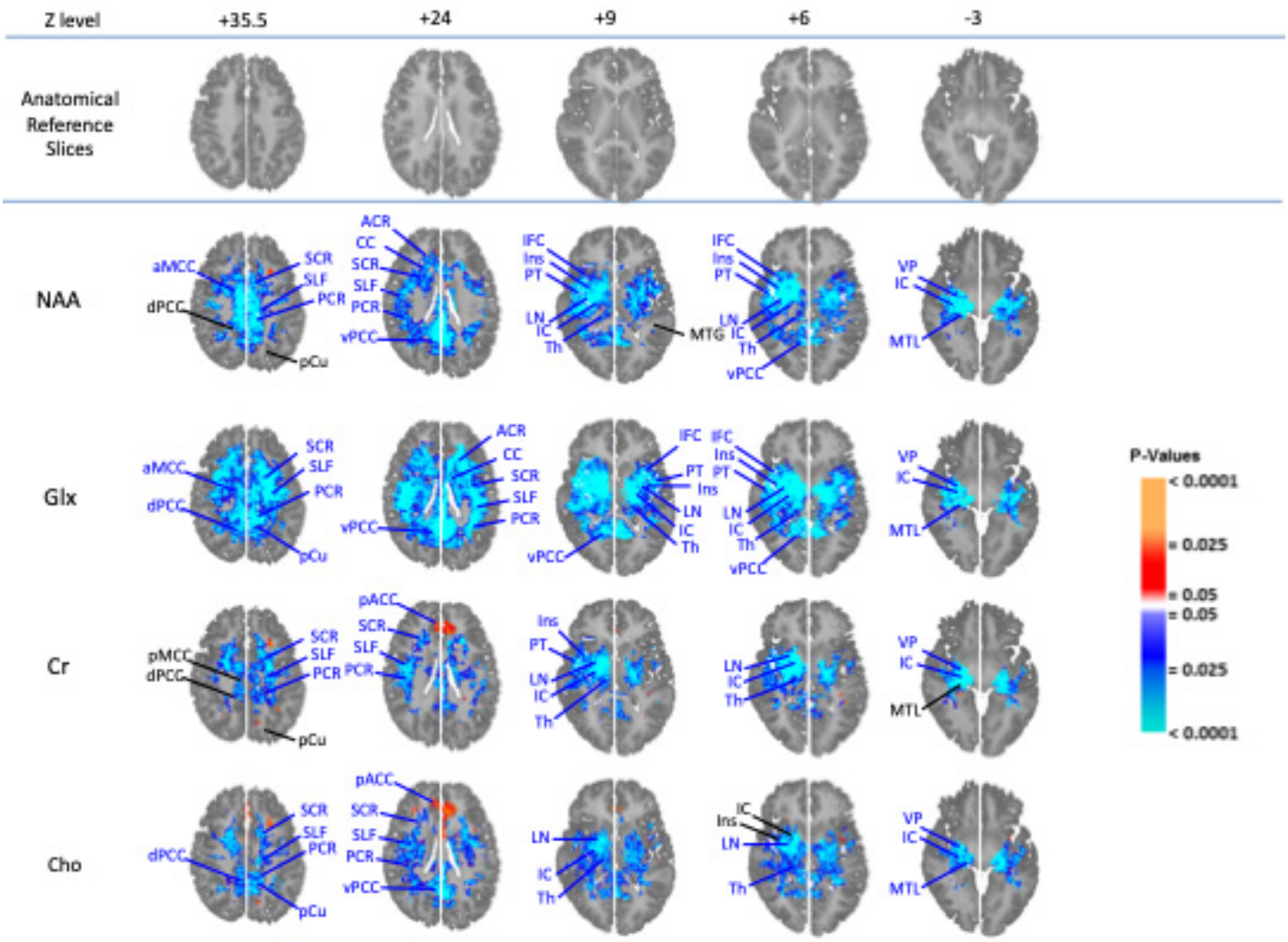

Figure S8 (B) Correlations showing main effects of age on metabolites within ASD sample covarying for sex and use of any psychotropic medication (FDR corrected); 78 ASD participants. To facilitate interpretation, each site that had a significant age-by-diagnosis interaction on panel (A) is reproduced here (black arrows and labels) regardless of whether or not it was accompanied by a significant main effect of age. Blue arrows and labels indicate additional sites where there was a significant main effect of age in the absence of a significant interaction. ACR, anterior corona radiata; aMCC, anterior middle cingulate cortex; CC, corpus callosum; IFC, inferior frontal cortex; LN, lenticular nucleus; PCR, posterior corona radiata; PT, planum temporale; SCR, superior corona radiata; SLF, superior longitudinal fasciculus; Th, thalamus; VP, ventral pallidum; vPCC, ventral posterior cingulate cortex.

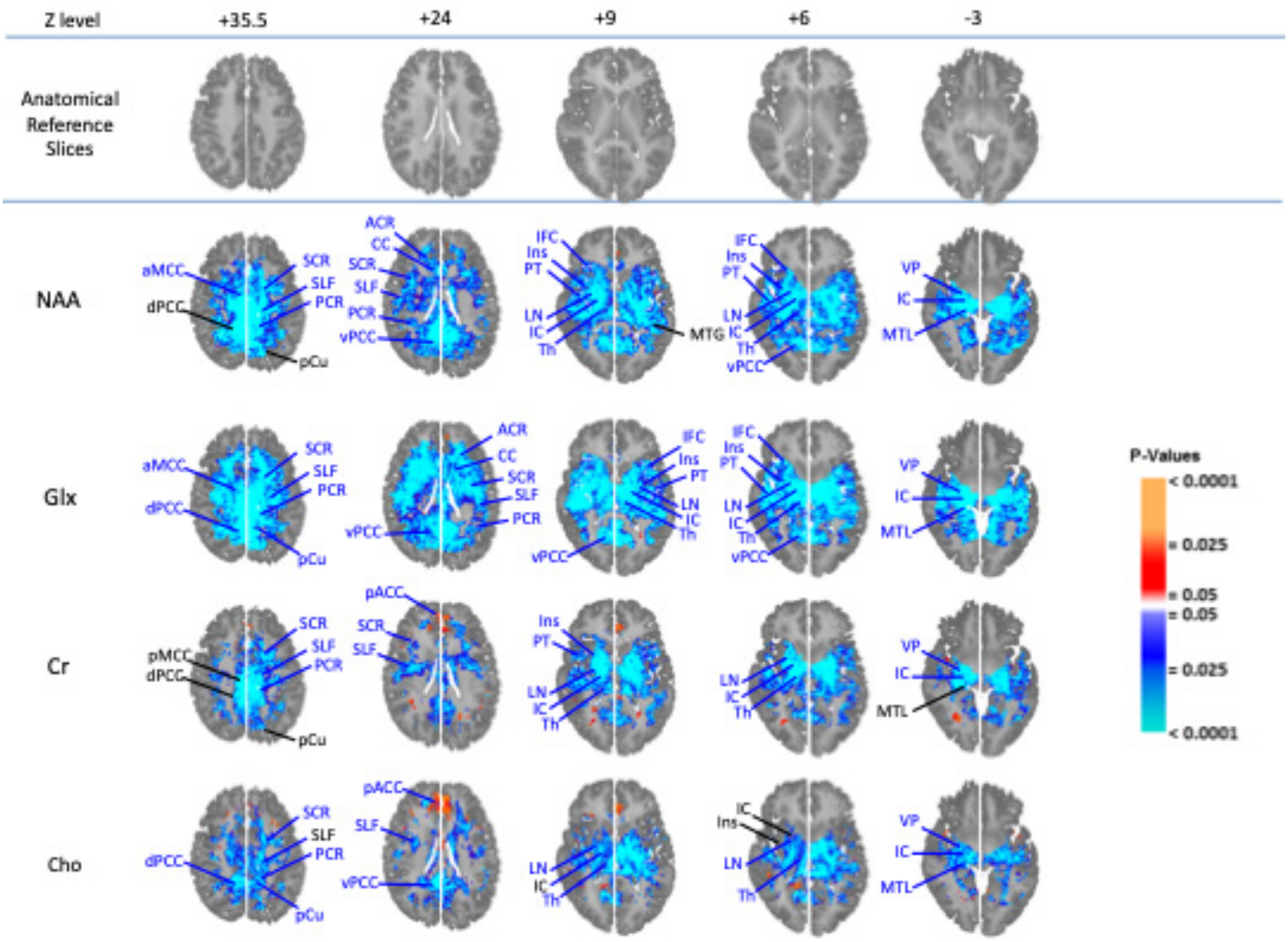

Figure S8 (C) Correlations showing main effects of age on metabolites within TD sample covarying for sex (FDR-corrected); 86 control participants. Sites with a significant age-by-diagnosis interaction on panel (A) are reproduced with black arrows and labels; blue arrows and labels indicate additional sites with a significant main effect of age.

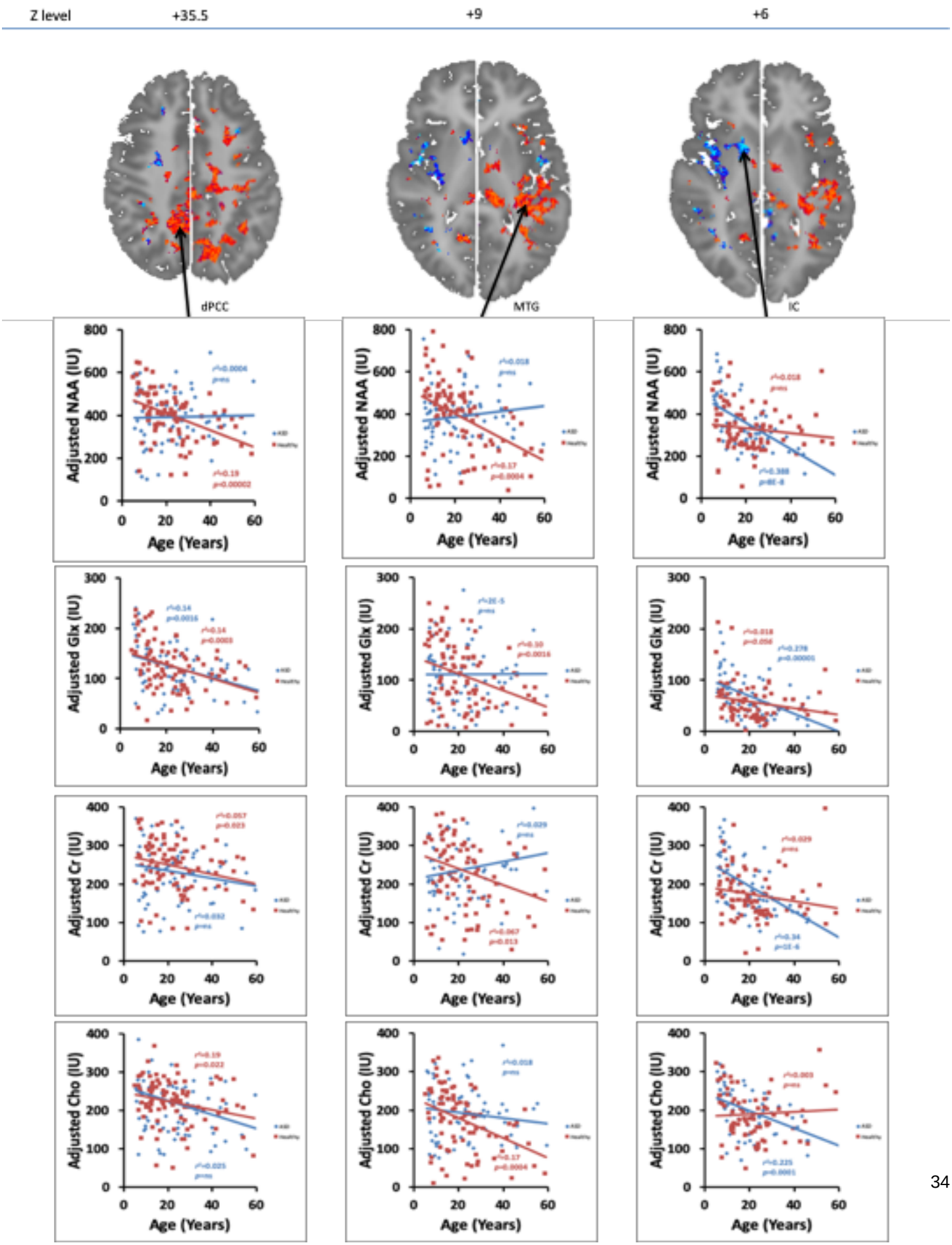
Z level
+35.5
+9
+6
dPCC
MTG
IC
Adjusted NAA (IU)
Adjusted Glx (IU)
Adjusted Cr (IU)
Adjusted Cho (IU)
Age (Years)

Figure S8 (D) Meanings of the age-by-diagnosis interactions. For metabolite NAA, at three representative anatomic points (voxels) from panel (A), scatterplots from the data of panels (B) and (C) are shown below to indicate the variation of NAA (corrected for sex and use of any psychotropic medication) with age in the separate ASD and TD samples. The positive age-by-diagnosis interaction (left) in right dPCC corresponds to an absence in ASD of the normal age-related decline in NAA in TD in this and other regions. This is also seen in left MTG (center). The negative age-by-diagnosis interaction (right) in right IC corresponds to a steeper decline in NAA with increasing age in ASD than in TD. Below are similar plots for Glx, Cr, and Cho. Homoscedasticity was affirmed by refitting the scatterplots after semi-log transform. Possible nonlinear effects of age on metabolite levels were assessed by adding an age^2 term to the model. While the age^2 effect was, in some cases, weakly significant, the first-order age-term remained dominant and the direction of effects was unchanged. The linear model was therefore retained for simplicity.

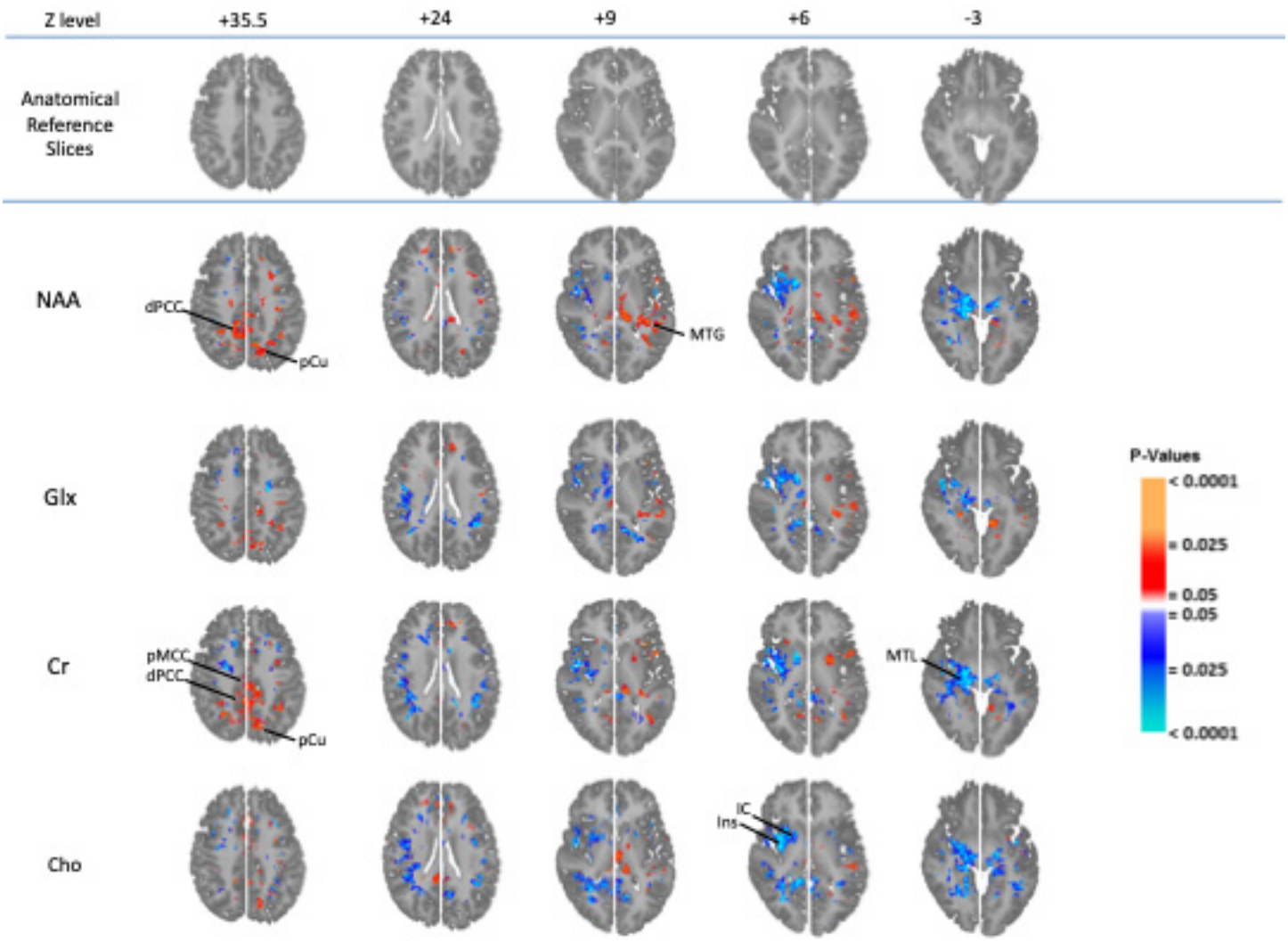

Figure S9 (A) Age-by-diagnosis interactions covarying for sex and diagnosis (FDR-corrected); 52 unmedicated ASD, 96 control participants. NAA, *N*-acetyl-compounds; Glx, glutamate plus glutamine; Cr, creatine plus phosphocreatine; Cho, choline compounds. dPCC, dorsal posterior cingulate cortex; IC, internal capsule; Ins, insula; MTG, middle temporal gyrus; MTL, mesial temporal lobe; pCu, precuneus; pMCC, posterior middle cingulate cortex.

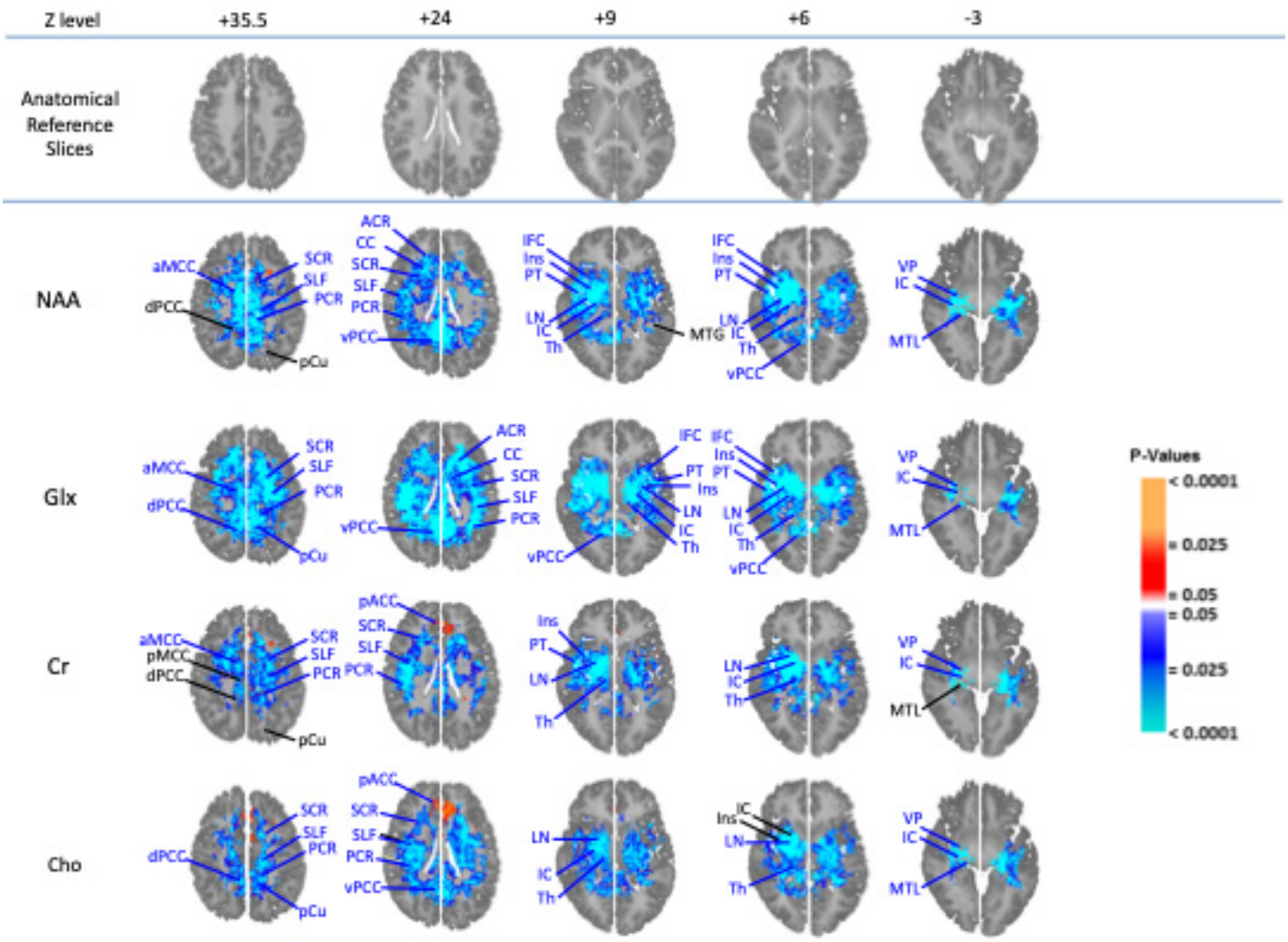

Figure S9 (B) Correlations showing main effects of age on metabolites within unmedicated ASD sample covarying for sex (FDR-corrected); 52 unmedicated ASD participants. Sites with a significant age-by-diagnosis interaction on panel (A) are reproduced with black arrows and labels; blue arrows and labels indicate additional sites with a significant main effect of age. ACR, anterior corona radiata; aMCC, anterior middle cingulate cortex; CC, corpus callosum; IFC, inferior frontal cortex; LN, lenticular nucleus; PCR, posterior corona radiata; PT, planum temporale; SCR, superior corona radiata; SLF, superior longitudinal fasciculus; Th, thalamus; VP, ventral pallidum; vPCC, ventral posterior cingulate cortex.

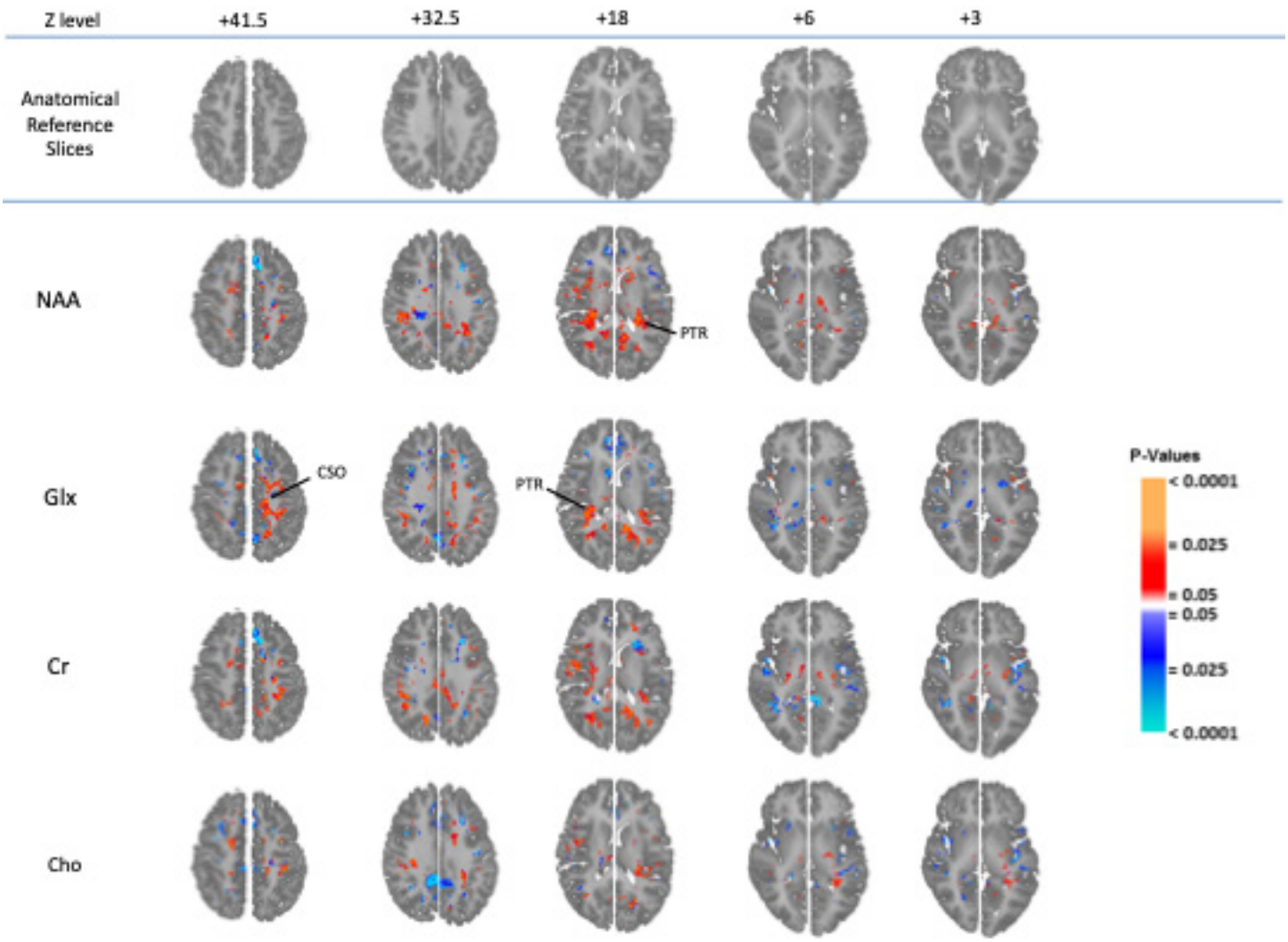

Figure S10 (A) Sex-by-diagnosis interactions for metabolites covarying for age, sex, diagnosis and use of any psychotropic medication (FDR-corrected); 78 (63 male/15 female) ASD, 96 (69 male/27 female) control participants. NAA, *N*-acetyl-compounds; Glx, glutamate plus glutamine; Cr, creatine plus phosphocreatine; Cho, choline compounds. CSO, centrum semiovale; PTR, posterior thalamic radiations.

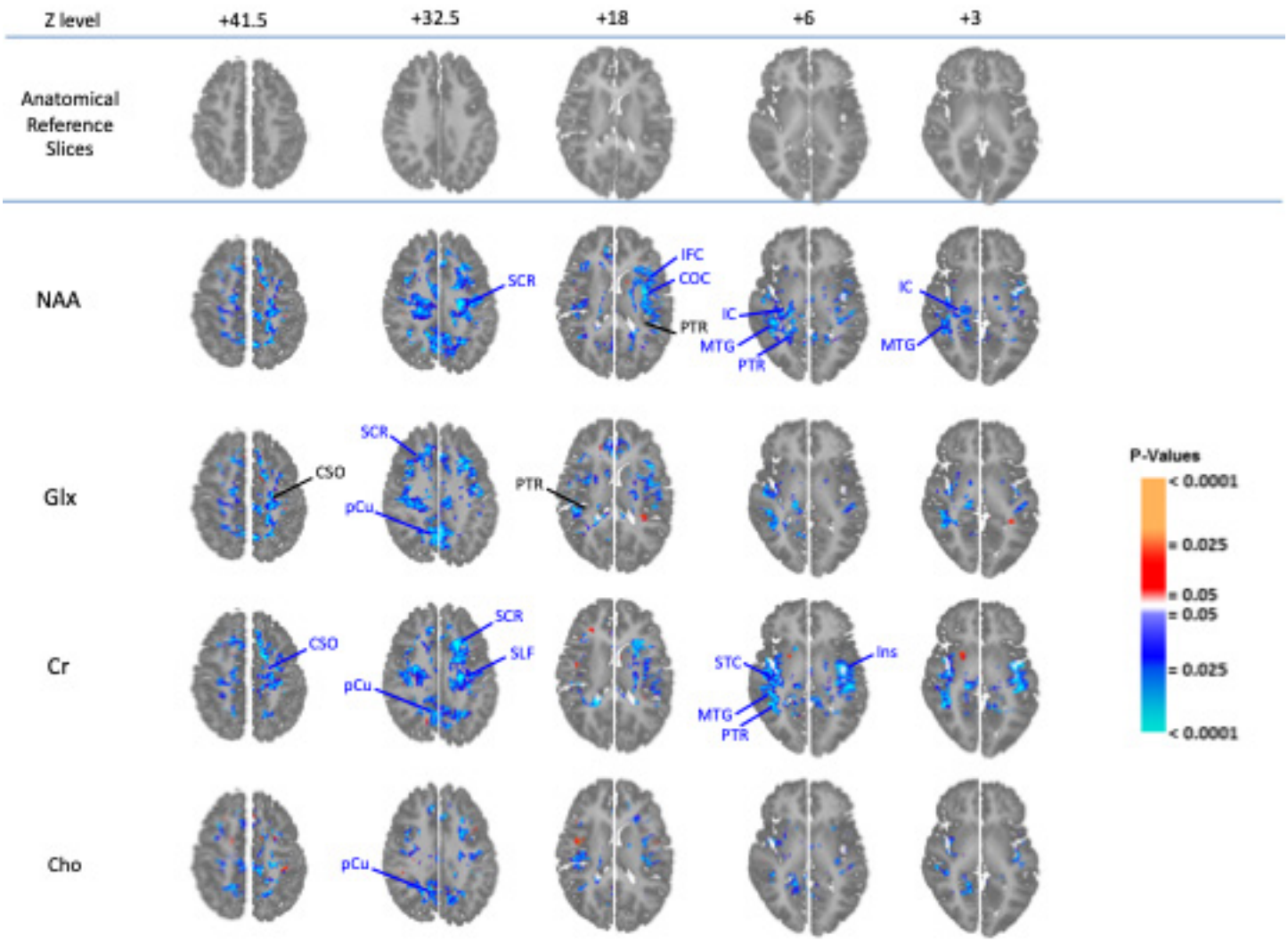

Figure S10 (B) Main effect of sex on metabolites within ASD sample. Brain regions where metabolites are higher (orange-red) or lower (cyan-blue) in male than in female participants covarying for age and use of any psychotropic medication (FDR-corrected); 78 (63 male/15 female) ASD participants. Sites with a significant sex-by-diagnosis interaction on panel (A) are reproduced with black arrows and labels; blue arrows and labels indicate additional sites with a significant main effect of sex. COC, central opercular cortex; dPCC, dorsal posterior cingulate cortex; IC, internal capsule; IFC, inferior frontal cortex; MTG, middle temporal gyrus; pCu, precuneus; PTR, posterior thalamic radiations; SCR, superior corona radiata; SLF, superior longitudinal fasciculus; STC, superior temporal cortex.

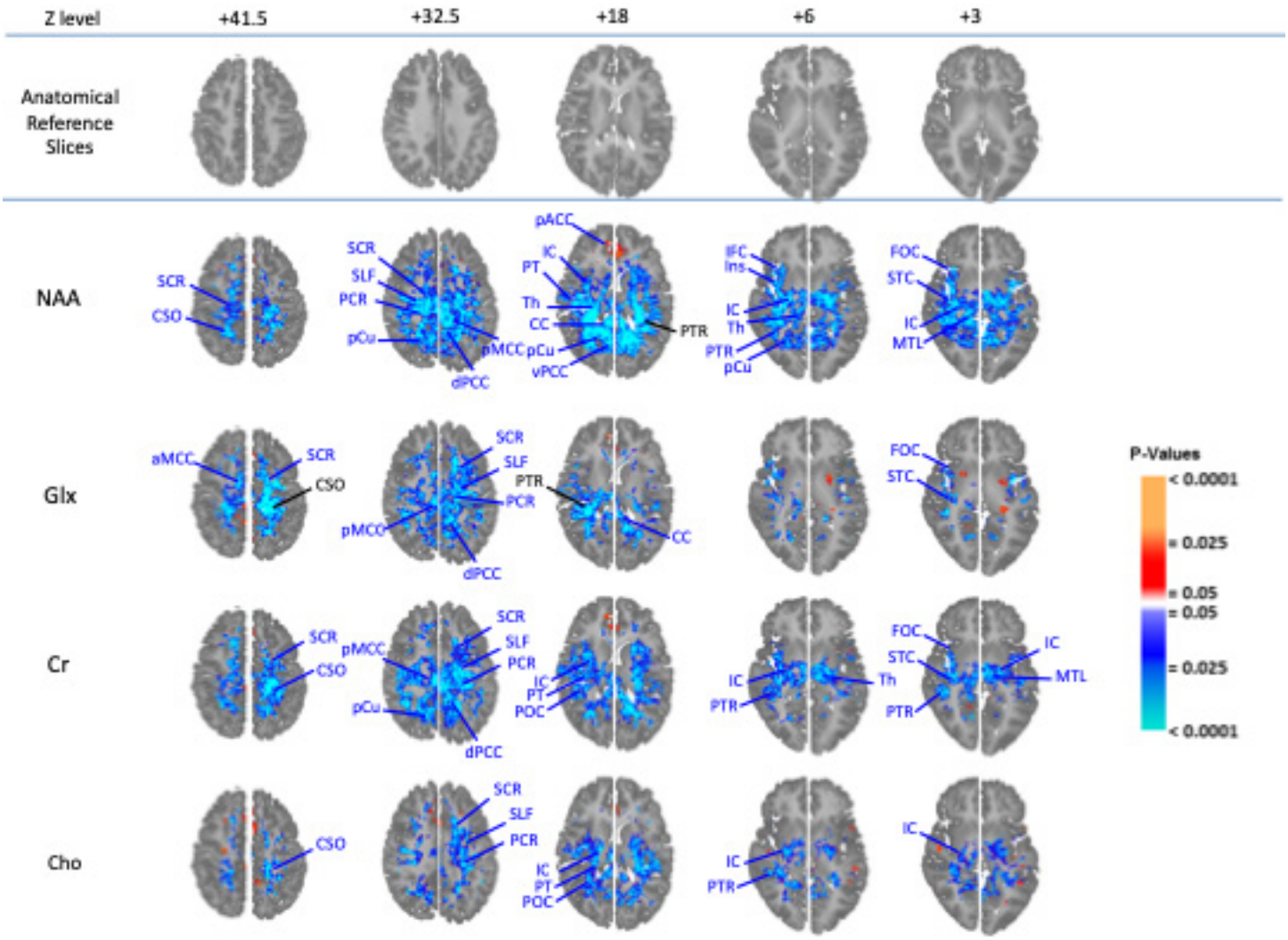

Figure S10 (C) Main effect of sex on metabolites within TD sample. Brain regions where metabolites are higher (orange-red) or lower (cyan-blue) in male than in female participants covarying for age (FDR-corrected); 96 (69 male/27 female) control participants. Sites with a significant sex-by-diagnosis interaction on panel (A) are reproduced with black arrows and labels; blue arrows and labels indicate additional sites with a significant main effect of sex. CC, corpus callosum; FOC, frontal opercular cortex; IC, internal capsule; Ins, insula; MTL, mesial temporal lobe; pACC, pregenual anterior cingulate cortex; PCR, posterior corona radiata; pMCC, posterior middle cingulate cortex; POC, parietal opercular cortex; PT, planum temporale; Th, thalamus; vPCC, ventral posterior cingulate cortex.

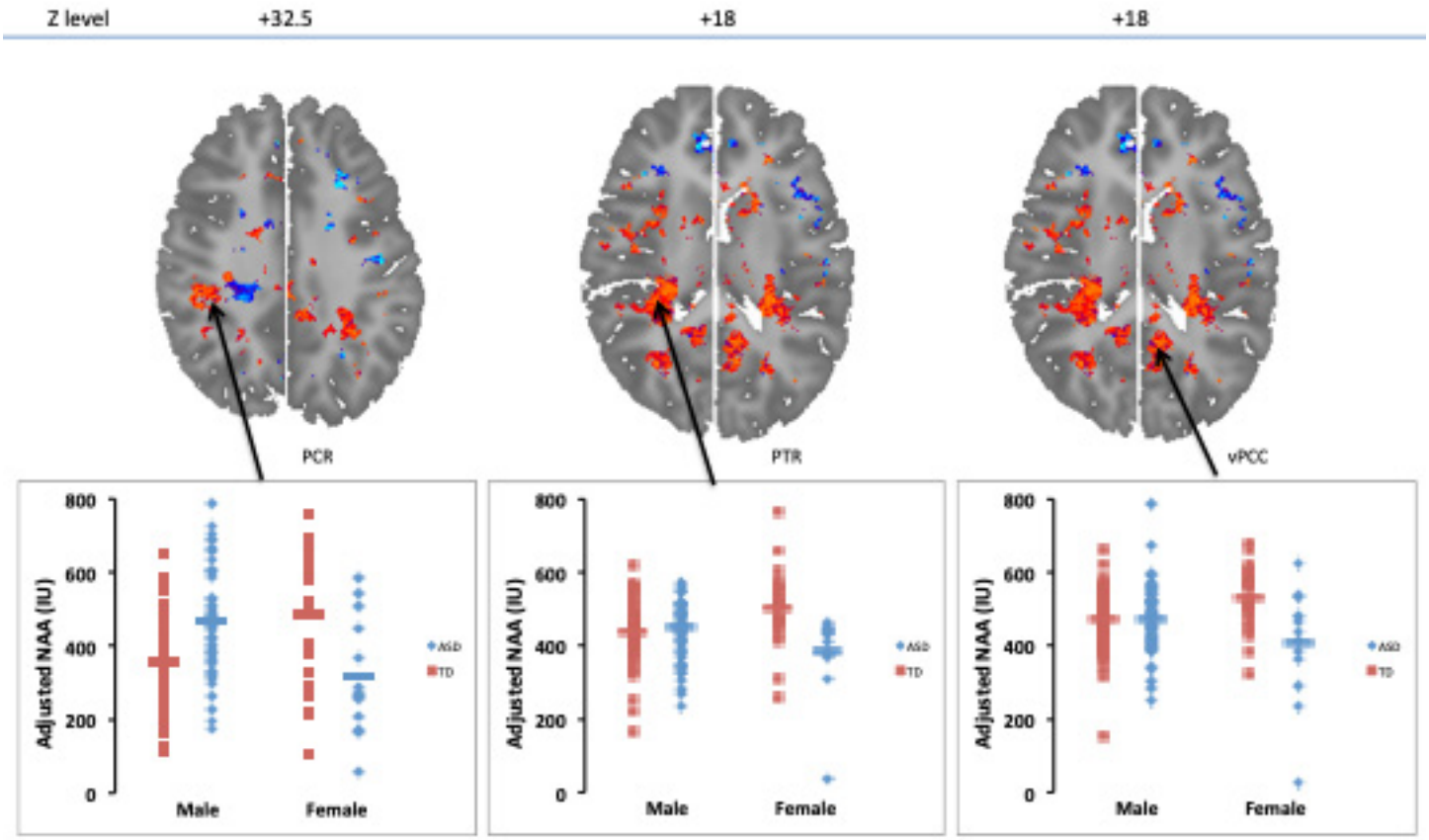

Figure S10 (D) Meanings of the sex-by-diagnosis interactions. For metabolite NAA, at three selected representative voxels from panel (A), scatterplots from the data of panels (B) and (C) are shown below to indicate male-female differences in NAA (corrected for age and use of any psychotropic medication) in the separate ASD and TD samples. The positive age-by-diagnosis interaction (left) in right PCR corresponds to higher mean NAA in males *vs.* females in the ASD sample, but lower NAA in males *vs.* females in the TD sample. This is also seen in right PTR (center) and left vPCC (right). Also note overall that female ASD NAA levels are roughly comparable to TD male levels, consistent with the female brain in ASD being akin to the male. Below are similar plots for Glx, Cr, and Cho.

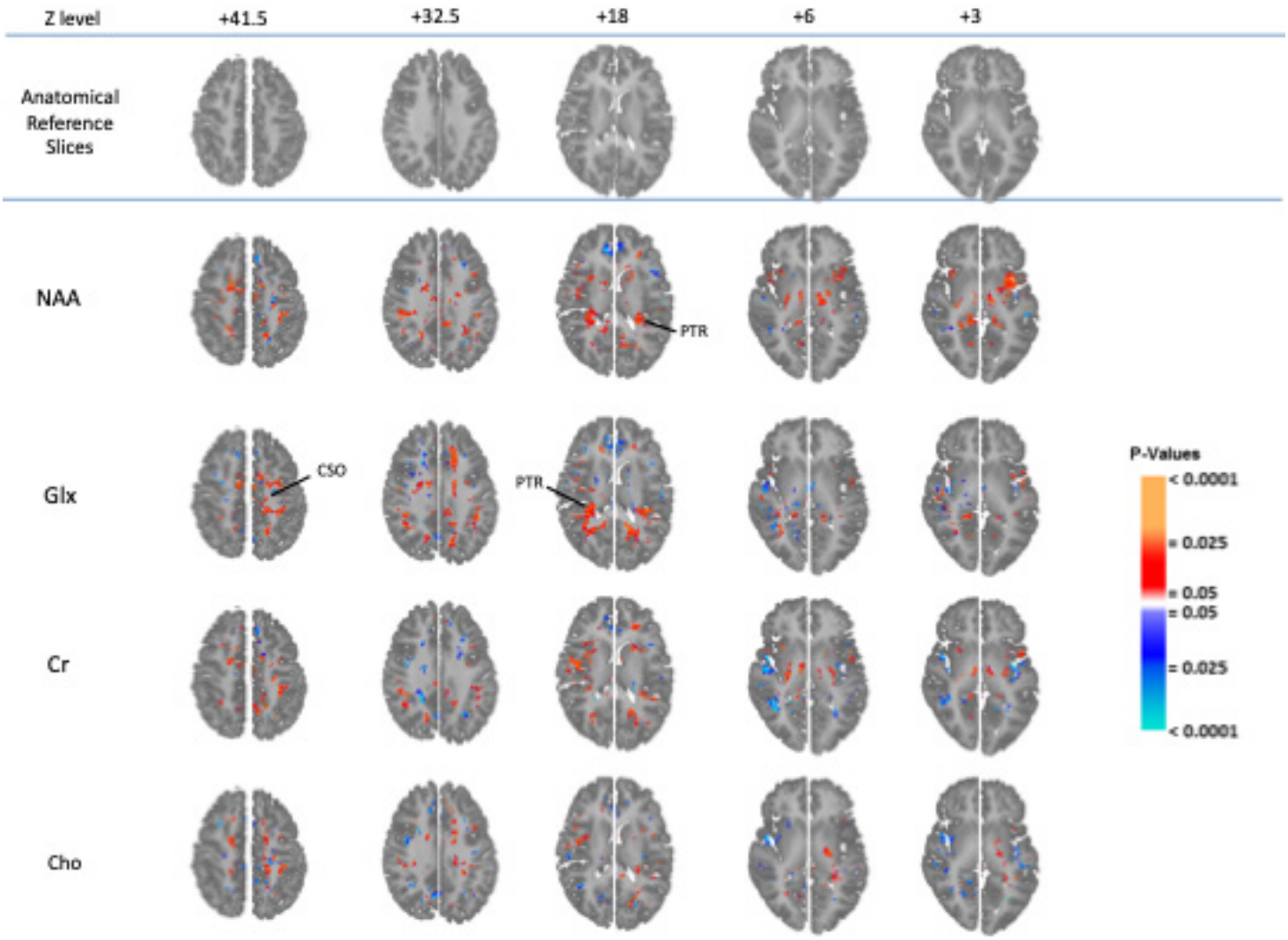

Figure S11 (A) Sex-by-diagnosis interactions covarying for age, sex, diagnosis (FDR-corrected); 52 (42 male/10 female) unmedicated ASD, 96 (69 male/27 female) control participants. NAA, *N*-acetyl-compounds; Glx, glutamate plus glutamine; Cr, creatine plus phosphocreatine; Cho, choline compounds. CSO, centrum semiovale; PTR, posterior thalamic radiations.

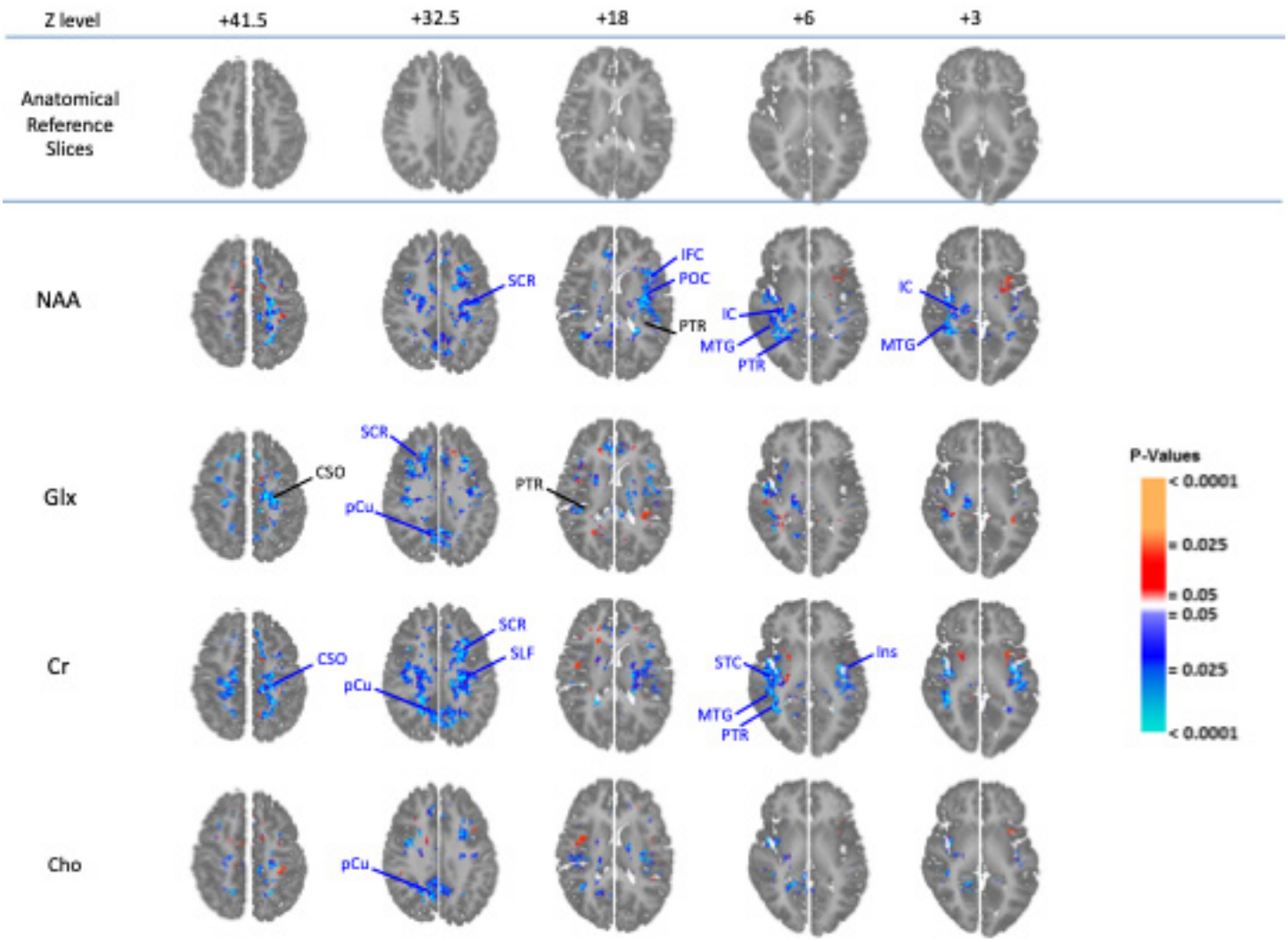

Figure S11 (B) Main effects of sex on metabolites within unmedicated ASD sample. Brain regions where metabolite levels are higher (orange-red) or lower (cyan-blue) in male than in female participants accounting for age (FDR-corrected); 52 (42 male/10 female) unmedicated ASD participants. Sites with a significant sex-by-diagnosis interaction on panel (A) are reproduced with black arrows and labels; blue arrows and labels indicate additional sites with a significant main effect of sex. IC, internal capsule; IFC, inferior frontal cortex; Ins, insula; MTG, middle temporal gyrus; pCu, precuneus; POC, parietal opercular cortex; PTR, posterior thalamic radiations; SCR, superior corona radiata; SLF, superior longitudinal fasciculus; STC, superior temporal cortex.

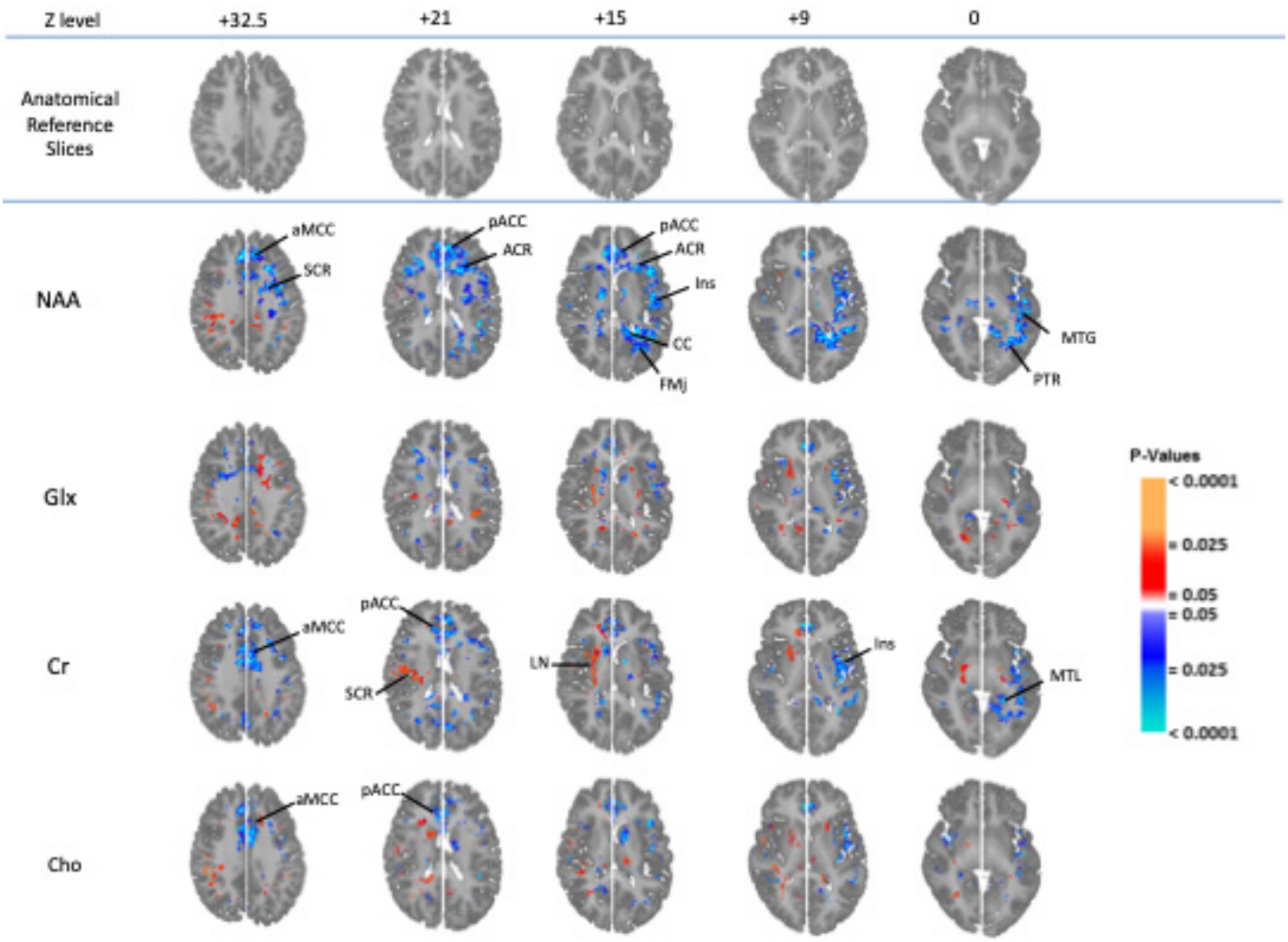

Figure S12 (A) Regions where metabolite levels are higher (orange-red) and lower (cyan-blue) for the ASD than the control sample, covarying for age and use of any psychotropic medication (FDR-corrected); 63 male ASD and 69 male control participants. ACR, anterior corona radiata; aMCC, anterior middle cingulate cortex; CC, corpus callosum; Ins, insula; FMj, forceps major; LN, lenticular nucleus; MTG, middle temporal gyrus; MTL, mesial temporal lobe; pACC, pregenual anterior cingulate cortex; PTR, posterior thalamic radiations; SCR, superior corona radiata.

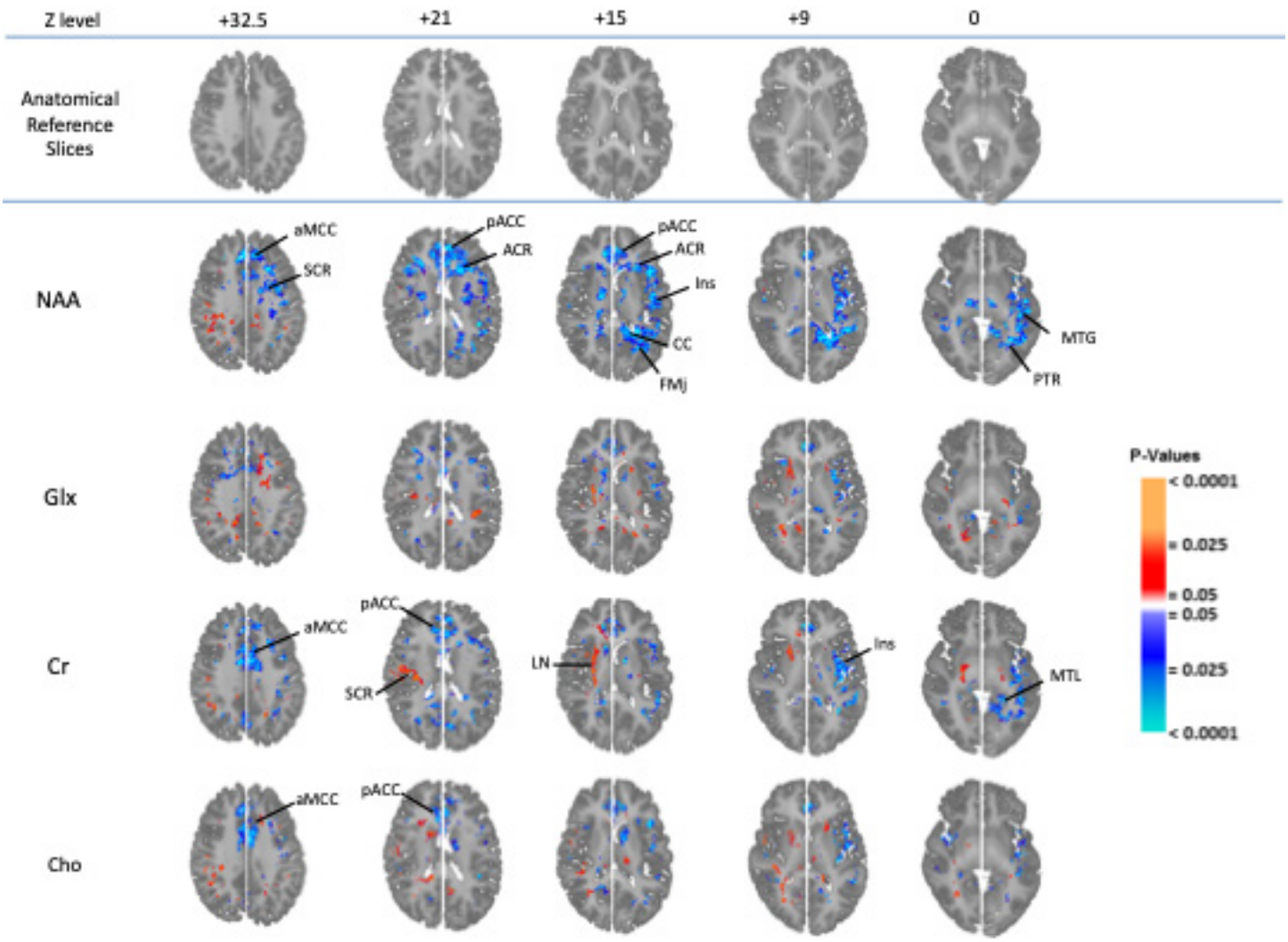

Figure S12 (B) Regions where metabolite levels are higher (orange-red) and lower (cyan-blue) for the ASD than the control sample, covarying for age (FDR-corrected); 42 unmedicated male ASD and 69 male control participants.

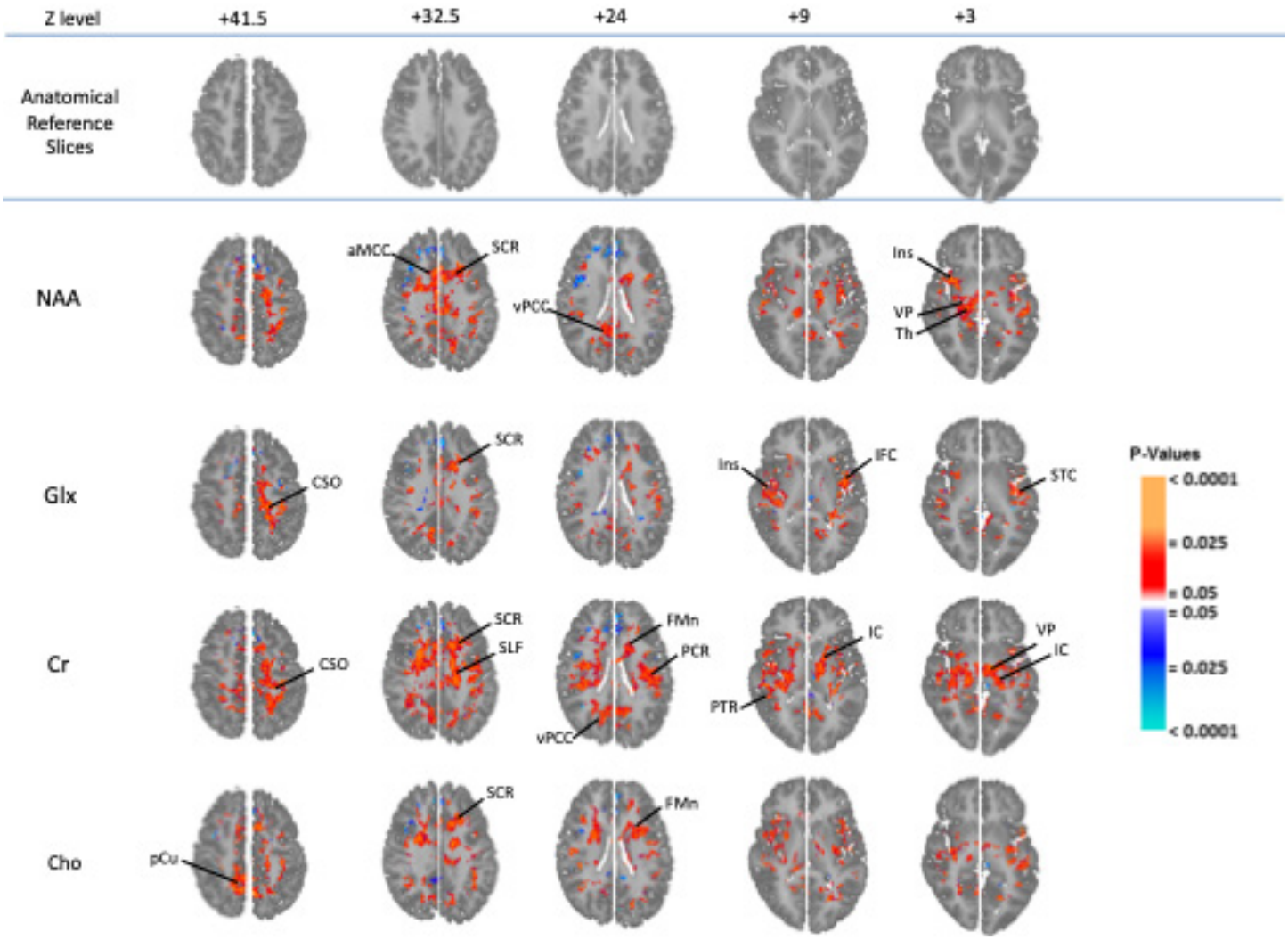

Figure S13 (A) FSIQ-by-diagnosis interactions for metabolites covarying for age, sex, diagnosis, FSIQ and use of any psychotropic medication (FDR-corrected); 68 ASD, 93 control participants. NAA, *N*-acetyl-compounds; Glx, glutamate plus glutamine; Cr, creatine plus phosphocreatine; Cho, choline compounds. aMCC, anterior middle cingulate cortex; CSO, centrum semiovale; FMn, forceps minor; IC, internal capsule; IFC, inferior frontal cortex; Ins, insula; pCu, precuneus; PCR, posterior corona radiata; PTR, posterior thalamic radiations; SCR, superior corona radiata; SLF, superior longitudinal fasciculus; STC, superior temporal cortex; Th, thalamus; VP, ventral pallidum; vPCC, ventral posterior cingulate cortex.

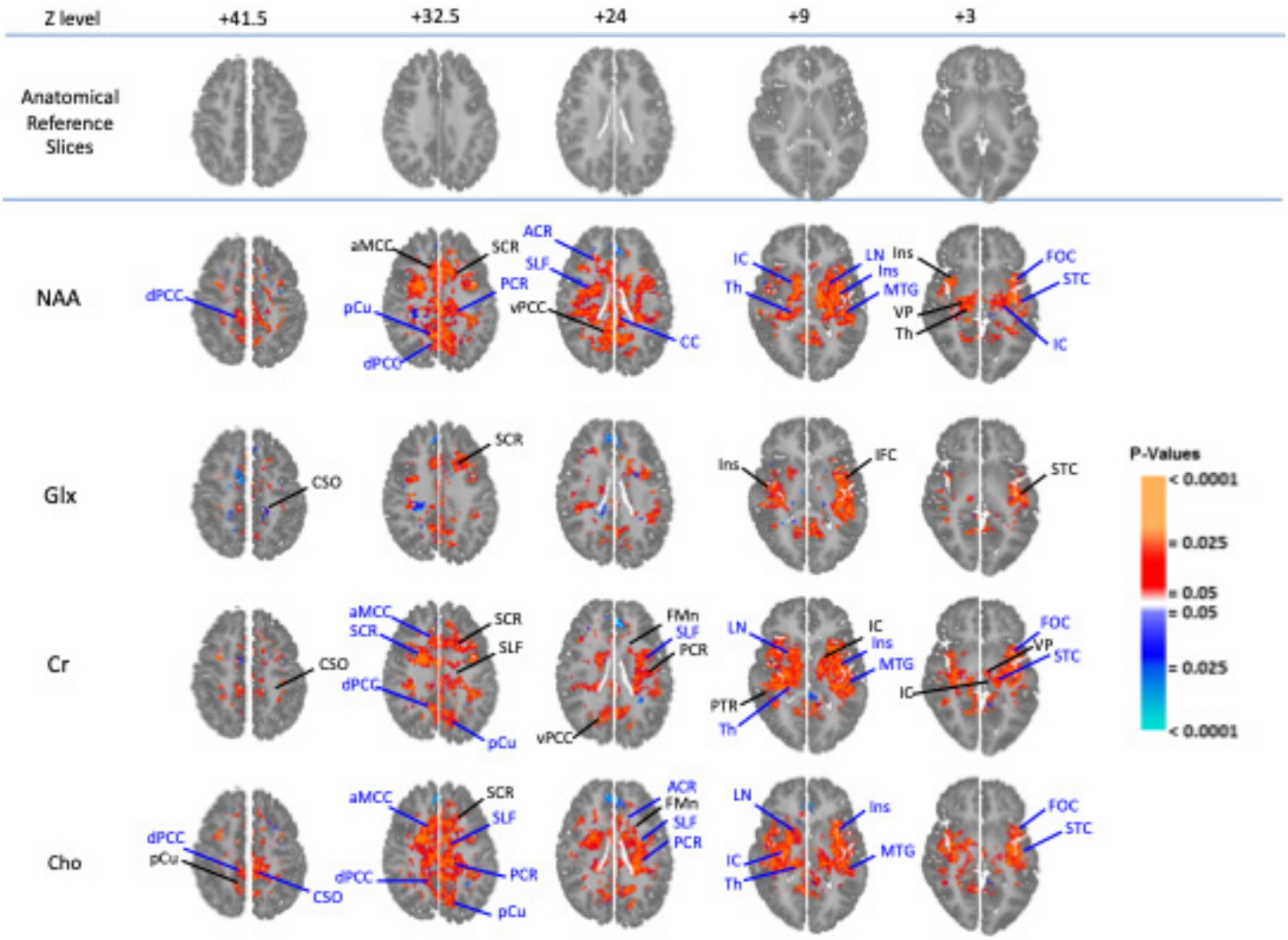

Figure S13 (B) Correlations showing main effect of FSIQ on metabolites within ASD sample covarying for age, sex and use of any psychotropic medication (FDR-corrected); 68 ASD participants. Sites with a significant FSIQ-by-diagnosis interaction on panel (A) are reproduced with black arrows and labels; blue arrows and labels indicate additional sites with a significant main effect of FSIQ. ACR, anterior corona radiata; CC, corpus callosum; dPCC, dorsal posterior cingulate cortex; FOC, frontal opercular cortex; LN, lenticular nucleus; MTG, middle temporal gyrus; POC, parietal opercular cortex.

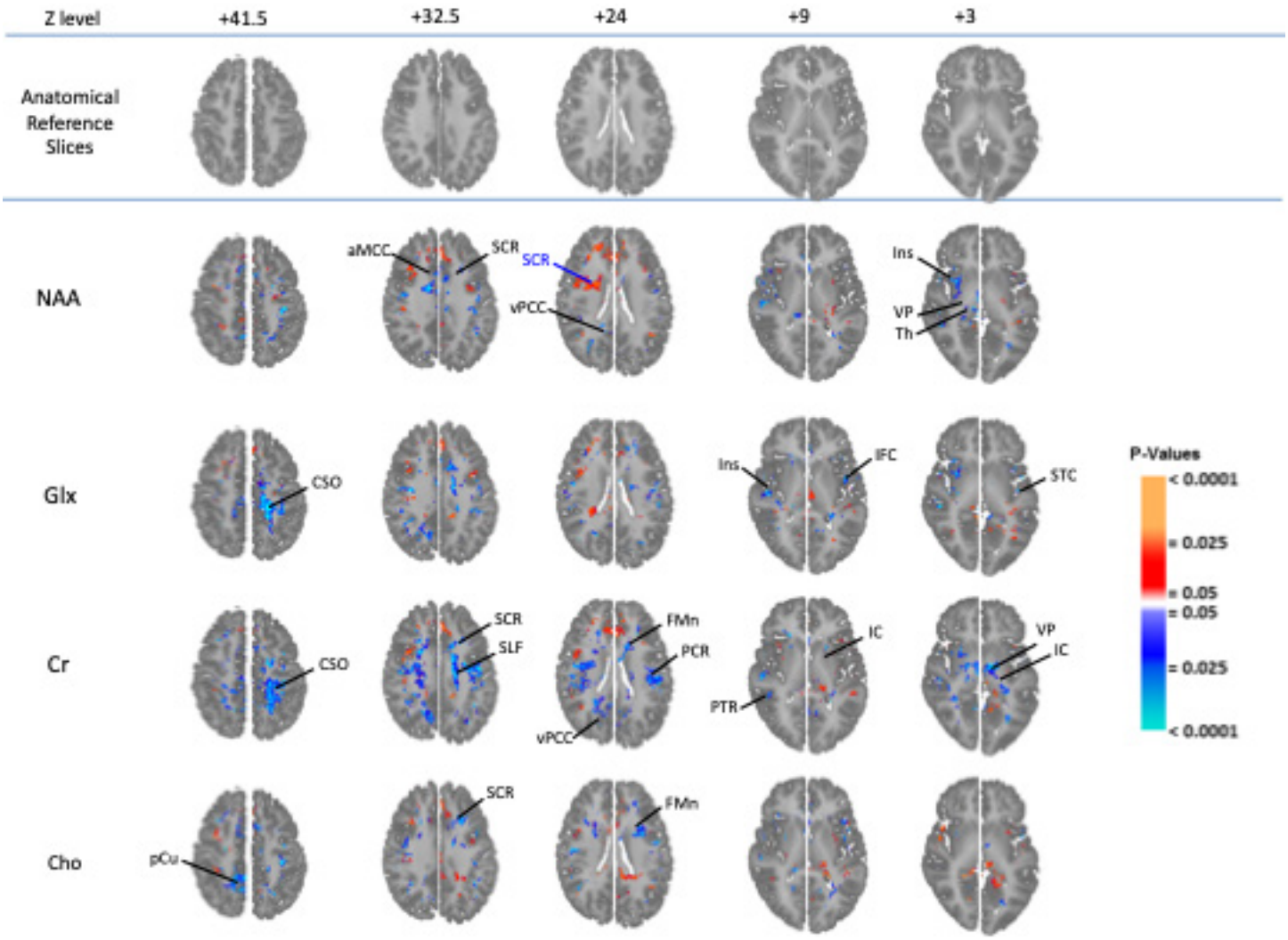

Figure S13 (C) Correlations showing main effect of FSIQ on metabolites within TD sample covarying for age and sex (FDR-corrected); 93 control participants. Sites with a significant FSIQ-by-diagnosis interaction on panel (A) are reproduced with black arrows and labels; blue arrows and labels indicate additional sites with a significant main effect of FSIQ.

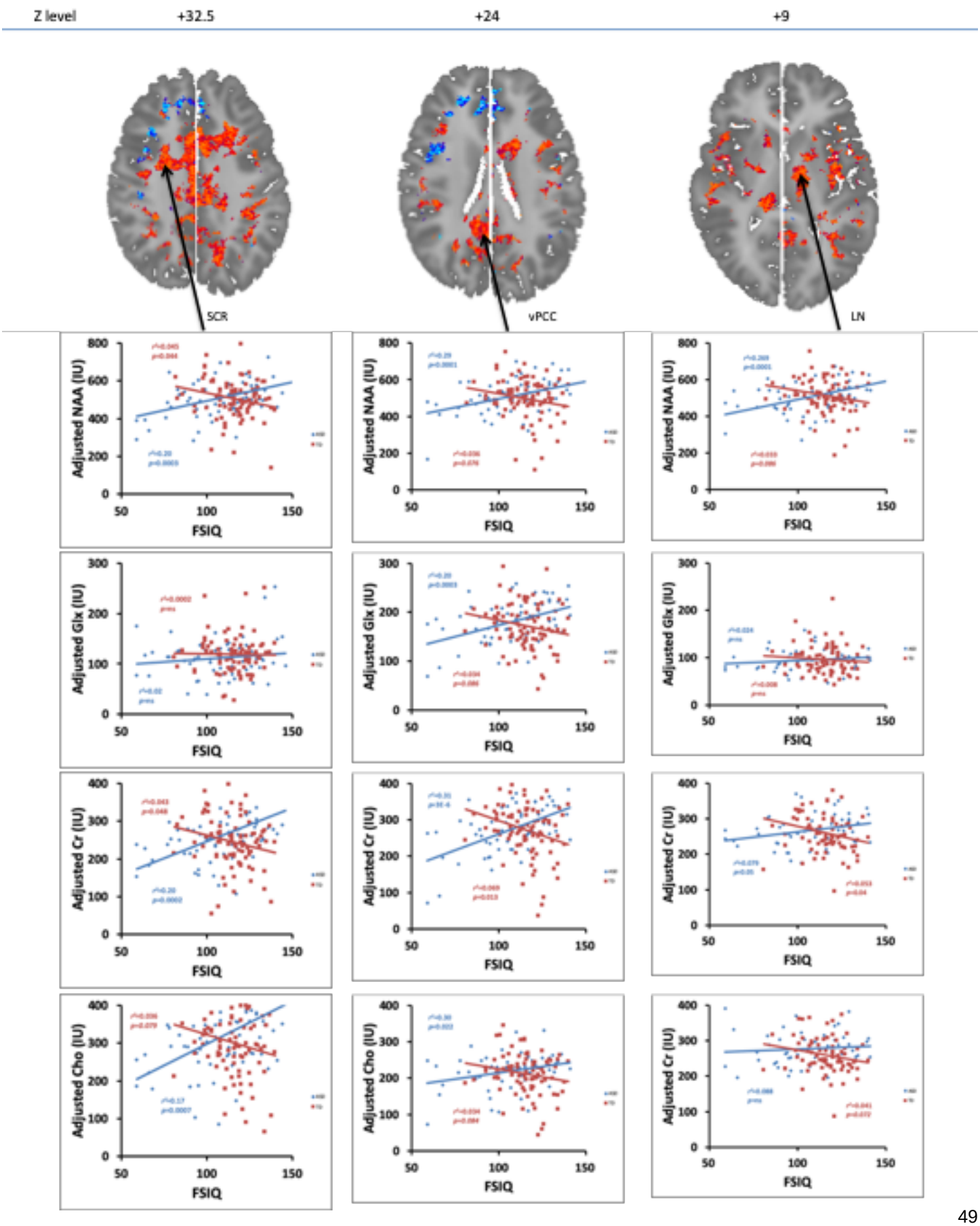
Z level
+32.5
+24
+9
SCR
vPCC
LN
Adjusted NAA (IU)
Adjusted Glx (IU)
Adjusted Cr (IU)
Adjusted Cho (IU)
FSIQ

Figure S13 (D) Meanings of the FSIQ-by-diagnosis interactions. For metabolite NAA, at three selected representative voxels from panel (A), scatterplots from the data of panels (B) and (C) are shown below to indicate the variation of NAA (corrected for age, sex and use of any psychotropic medication) with FSIQ in the separate ASD and TD samples. The positive FSIQ-by-diagnosis interaction (left) in right SCR corresponds to a decrease in NAA with decreasing FSIQ in ASD *vs.* an increase in NAA with decreasing FSIQ in TD. A similar pattern is seen in right vPCC (center) and in left LN (right). Thus, the NAA signature of lower IQ is opposite in ASD and TD. Below are similar plots for Glx, Cr, and Cho.

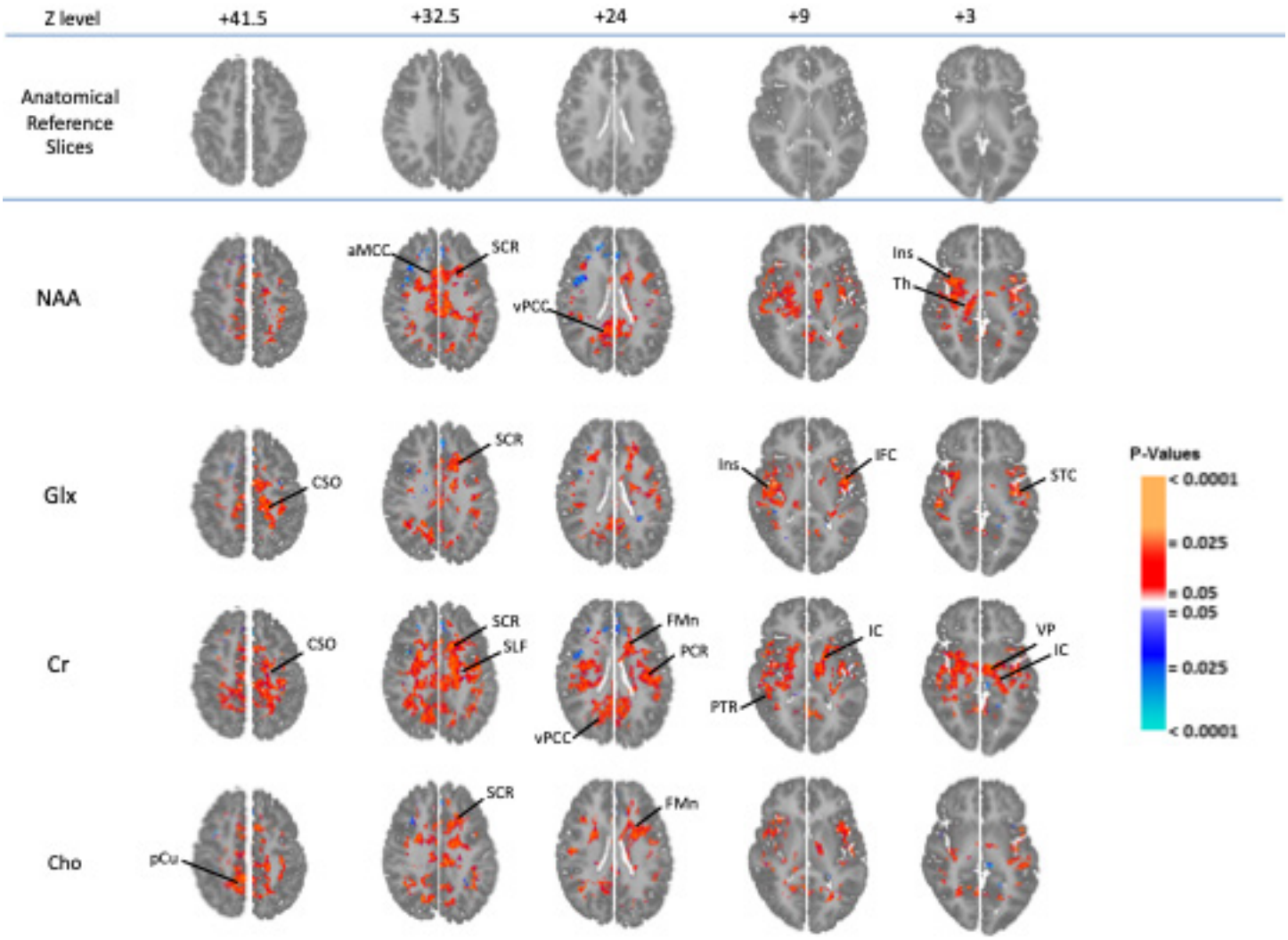

Figure S14 (A) FSIQ-by-diagnosis interactions covarying for age, sex, diagnosis and FSIQ (FDR-corrected); 44 unmedicated ASD, 93 control participants. NAA, *N*-acetyl-compounds; Glx, glutamate plus glutamine; Cr, creatine plus phosphocreatine; Cho, choline compounds. aMCC, anterior middle cingulate cortex; CSO, centrum semiovale; FMn, forceps minor; IC, internal capsule; IFC, inferior frontal cortex; Ins, insula; pCu, precuneus; PCR, posterior corona radiata; PTR, posterior thalamic radiations; SCR, superior corona radiata; SLF, superior longitudinal fasciculus; STC, superior temporal cortex; Th, thalamus; VP, ventral pallidum; vPCC, ventral posterior cingulate cortex.

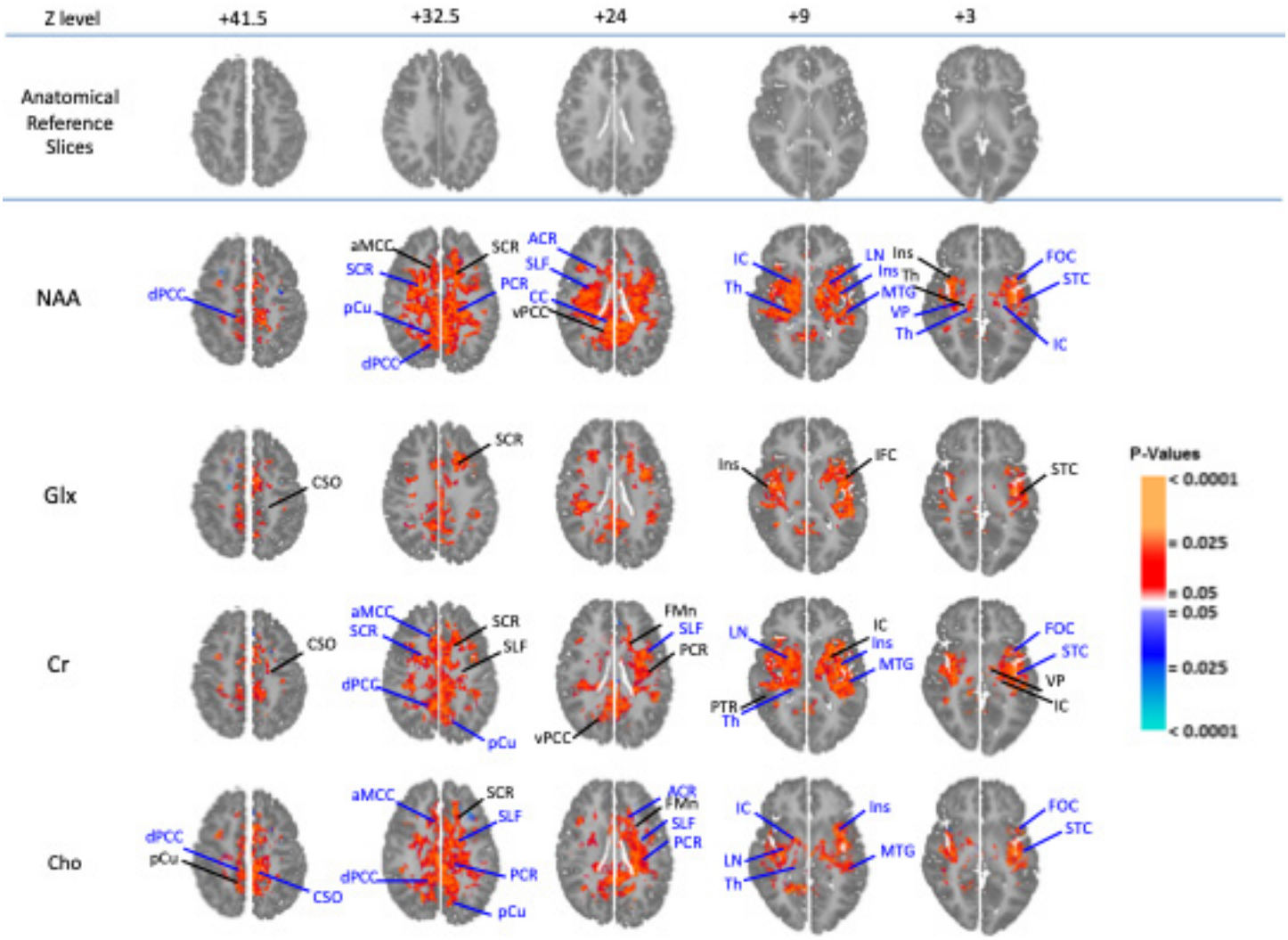

Figure S14 (B) Correlations showing main effect of FSIQ on metabolites within unmedicated ASD sample covarying for age and sex (FDR-corrected); 44 unmedicated ASD participants. Sites with a significant FSIQ-by-diagnosis interaction on panel (A) are reproduced with black arrows and labels; blue arrows and labels indicate additional sites with a significant main effect of FSIQ. ACR, anterior corona radiata; CC, corpus callosum; dPCC, dorsal posterior cingulate cortex; FOC, frontal opercular cortex; LN, lenticular nucleus; MTG, middle temporal gyrus.

Supplemental References

1. Goh S, Dong ZC, Zhang YD, DiMauro S, Peterson BS (2014): Mitochondrial dysfunction as a neurobiological subtype of autism spectrum disorder: Evidence from brain imaging. *JAMA Psychiatry* 71(6): 665-671.

2. Lord C, Rutter M, Le Couteur A (1994): Autism Diagnostic Interview: a revised version of a diagnostic interview for caregivers of individuals with possible pervasive developmental disorders. *J Autism Dev Disord* 24(5): 659-685.

3. Lord C, Risi S, Lambrecht L, Cook EH Jr, Leventhal BL, DiLavore PC, Pickles A, Rutter M (2000): The Autism Diagnostic Observation Schedule-Generic: a standard measure of social and communication deficits associated with the spectrum of autism. *J Autism Dev Disord* 30(3): 205-223.

4. Constantino JN (2002): *The Social Responsiveness Scale*. Los Angeles: Western Psychological Services.

5. Rutter M, Bailey A, Lord C (2003): *The Social Communication Questionnaire*. Los Angeles: Western Psychological Services.

6. Hartigan JA (1975): Clustering Algorithms. New York: Wiley.

7. Duyn JH, Gillen J, Sobering G, van Zijl PC, Moonen CT (1993): Multisection protonMR spectroscopic imaging of the brain. *Radiology* 188(1): 277-282.

8. Hao X, Xu D, Bansal R, Dong Z, Liu J, Wang Z, Kangarlu A, Liu F, Duan Y, Shova S, Gerber AJ, Peterson BS (2013): Multimodal magnetic resonance imaging: The coordinated use of multiple, mutually informative probes to understand brain structure and function. *Hum Brain Mapp* 34(2): 253-271.

9. O'Neill J, Dong Z, Bansal R, Ivanov I, Hao X, Desai J, Pozzi E, Peterson BS (2000): Proton chemical shift imaging of the brain in pediatric and adult developmental stuttering. *JAMA Psychiatry 74*(1): 85-94.

10. Sled GJ, Zijdenbos AP, Evans AC (1998): A nonparametric method for automatic correction of intensity nonuniformity in MRI data. *IEEE Trans Med Imaging* 17(1): 87-97.

11. Shattuck DW, Leahy RM (2002): BrainSuite: An automated cortical surface identification tool. *Med Image Analysis* 8(2): 129-142.

12. Viola P, Wells WM (1995): Alignment by maximization of mutual information. *IEEE Proc 5th Int Conf on Computer Vision*, Boston, June 20-23.

13. Christensen GE, Joshi SC, Miller MI (1997): Volumetric transformation of brain anatomy. *IEEE Trans Med Imaging* 16(6): 1369-1383.

14. Smith SM (2002): Fast robust automated brain extraction. Hum Brain Mapp 7(3): 143-155.

15. Dong ZC, Peterson B (2007): The rapid and automatic combination of proton MRSI data using multi-channel coils without water suppressionl. *MRI* 25(8): 1148-1154.

16. Dong ZC (2015): Proton MRS and MRSI of the brain without water suppression. *Prog NMR Spec* 86-87: 65-79.

17. Dong Z, Liu F, Kangarlu A, Peterson BS (2012): Metabolite mapping with extended brain coverage using a fast multisection MRSI pulse sequence and a multichannel coil. *Int J Biomed Imaging* 2012:8.

18. Plessen KJ, Bansal R, Zhu H, Whiteman R, Amat J, Quackenbush GA, Martin L, Durkin K, Blair C, Royal J, Hugdahl K, Peterson BS (2006): Hippocampus and amygdala morphology in attention-deficit/hyperactivity disorder. *Arch Gen Psychiatry* 63: 795–807.

19. Sanchez CE, Richards JE, Almli CR (2012): Age-specific MRI templates for pediatric neuroimaging. Dev Neuropsychol 37(5): 379–399.

20. Fillmore, PT (2015): Age-specific MRI brain and head templates for healthy adults from 20 through 89 years of age. Fron Aging Neuroscience 7(44): 1-14.

21. Bansal R, Hellerstein DJ, Sawardekar S, O'Neill J, Peterson BS. Effects of the antidepressant medication duloxetine on brain metabolites in persistent depressive disorder: A randomized, controlled trial. PLoS ONE (in press)

22. de Beer R, van den Boogaart A, van Ormondt D, Pijnappel WWF, den Hollander JA, Merien AJH, Luyten PR (1992): Application of time-domain fitting in the quantification of In vivo 'H spectroscopic imaging data sets. NMR Biomed 5: 171-178.

23. Mueller SG, Ebel A, Barakos J, Scanlon C, Cheong I, Finlay D, Garcia P, Weiner MW, Laxer KD (2011): Widespread extrahippocampal NAA/(Cr+Cho) abnormalities in TLE with and without mesial temporal sclerosis. J Neurol 258: 603-612.

24. Benjamini Y, Hochberg Y (1995): Controlling the false discovery rate - a practical and powerful approach to multiple testing. *J Roy Stat Soc B-Methodological* 57(1): 289-300.

25. O'Neill J, Sobel TL, Vogt BA (2009): Localizing cingulate subregions-of-interest in magnetic resonance images guided by cytological parcellations. In: Vogt BA, editor. Cingulate Neurobiology and Disease. Oxford: Oxford University Press, pp 587-617.